



The 2023 Outburst of the Gaia Alerted EXor Gaia23bab

Zsófia Nagy^{1,2} , Ágnes Kóspál^{1,2,3} , Péter Ábrahám^{1,2,3,4} , Teresa Giannini⁵ , Mária Kun^{1,2} , Manuele Gangi^{5,6} , Fernando Cruz-Sáenz de Miera^{1,2,7} , Michael Kuhn⁸ , Michał Siwak^{1,2,9} , Máté Szilágyi^{1,2} , Eleonora Fiorellino^{10,11} , Simone Antoniucci⁵ , Katia Biazzo⁵ , Attila Bódi^{1,2,12} , Zsófia Bora^{1,2,3} , Borbála Cseh^{1,2,13} , Marek Drózd⁹ , Ágoston Horti-Dávid^{1,2,3} , András Péter Joó^{1,2,3} , Csilla Kalup^{1,2,3} , Krzysztof Kotysz¹⁴ , Levente Kriskovics^{1,2} , Gábor Marton^{1,2} , Przemysław J. Mikołajczyk^{14,15} , Brunella Nisini⁵ , András Pál^{1,2} , Bálint Seli^{1,2,3} , Ádám Sódor^{1,2} , László Szabados^{1,2} , Norton Olivér Szabó^{1,2,3} , Zsófia Marianna Szabó^{1,2,16,17} , Róbert Szakáts^{1,2} , Vázsony Varga^{1,2,3} , József Vinkó^{1,2,3} , Łukasz Wyrzykowski¹⁵ , and Paweł Zieliński¹⁸

¹ Konkoly Observatory, HUN-REN Research Centre for Astronomy and Earth Sciences Konkoly-Thege Miklós út 15-17, H-1121 Budapest, Hungary; nagy.zsofia@csfk.org

² CSFK, MTA Centre of Excellence, Konkoly-Thege Miklós út 15-17, 1121 Budapest, Hungary

³ ELTE Eötvös Loránd University, Institute of Physics and Astronomy, Pázmány Péter sétány 1A, Budapest 1117, Hungary

⁴ Department of Astrophysics, University of Vienna, Türkenschanzstr. 17, 1180, Vienna, Austria

⁵ INAF-Osservatorio Astronomico di Roma, via di Frascati 33, 00078, Monte Porzio Catone, Italy

⁶ ASI, Italian Space Agency, Via del Politecnico snc, 00133 Rome, Italy

⁷ Institut de Recherche en Astrophysique et Planétologie, Université de Toulouse, UT3-PS, OMP, CNRS, 9 av. du Colonel Roche, 31028 Toulouse Cedex 4, France

⁸ Centre for Astrophysics Research, University of Hertfordshire, College Lane, Hatfield, AL10 9AB, UK

⁹ Mt. Suhora Astronomical Observatory, University of the National Education Commission, ul. Podchorążych 2, 30-084 Kraków, Poland

¹⁰ Instituto de Astrofísica de Canarias, IAC, Vía Látcea s/n, 38205 La Laguna (S.C.Tenerife), Spain

¹¹ Departamento de Astrofísica, Universidad de La Laguna, 38206 La Laguna (S.C.Tenerife), Spain

¹² Department of Astrophysical Sciences, Princeton University, 4 Ivy Lane, Princeton, NJ 08544, USA

¹³ MTA-ELTE Lendület “Momentum” Milky Way Research Group, Budapest, Hungary

¹⁴ Astronomical Institute, University of Wrocław, ul. M. Kopernika 11, 51-622 Wrocław, Poland

¹⁵ Warsaw University Observatory, Al. Ujazdowskie 4, 00-478 Warsaw, Poland

¹⁶ Max Planck Institute for Radio Astronomy, Auf dem Hügel 69, 53121 Bonn, Germany

¹⁷ Scottish Universities Physics Alliance (SUPA), School of Physics and Astronomy, University of St Andrews, North Haugh, St Andrews, KY16 9SS, UK

¹⁸ Institute of Astronomy, Faculty of Physics, Astronomy and Informatics, Nicolaus Copernicus University in Toruń, ul. Grudzińska 5, 87-100 Toruń, Poland

Received 2024 September 13; revised 2025 April 26; accepted 2025 May 3; published 2025 June 25

Abstract

Episodic accretion is a fundamental process in the build-up of the stellar mass. EX Lupi-type eruptive young stars (EXors) represent one of the main types of episodic accretion. We study the recently discovered EXor Gaia23bab during its 2023 outburst. We obtained optical and near-infrared photometry and spectroscopy to probe the variation of the physical properties of Gaia23bab during its recent outburst. We also collected archival photometry to study a previous outburst of the star. We used several accretion tracers, including the Ca II triplet, He I, and various hydrogen lines from the Paschen and Brackett series, to measure the accretion rate during the outburst. The accretion rate is consistent with $\sim 2.0 \times 10^{-7} M_{\odot} \text{ yr}^{-1}$. Comparing the line fluxes of the hydrogen Brackett series to predictions of Case B theory suggests excitation temperatures of 5000–10,000 K and electron densities of 10^9 – 10^{10} cm^{-3} . Comparison to the predictions of a model for T Tauri stars revealed that the fluxes of the Balmer series are consistent with temperatures of 5000–12,500 K and a hydrogen density of 10^8 cm^{-3} , while the fluxes of the Paschen series are consistent with temperatures in the range between 10,000 and 12,500 K and a hydrogen density of 10^{11} cm^{-3} . The derived temperatures and densities confirm that Gaia23bab is a prototypical EXor, not only due to its accretion rate, but also based on the best-fit temperatures and densities revealed by the detected hydrogen lines.

Unified Astronomy Thesaurus concepts: Young stellar objects (1834); Classical T Tauri stars (252); Stellar accretion disks (1579); Pre-main sequence stars (1290); Eruptive variable stars (476); Star formation (1569)

1. Introduction

Low-amplitude short-term photometric variability (~ 0.2 mag over hours to weeks) has been detected in $\sim 50\%$ of young stellar objects (YSOs; S. T. Megeath et al. 2012). A subclass of YSOs, called young eruptive stars, shows much larger variability amplitudes of 2–5 mag at optical and infrared wavelengths on longer timescales, from months to a century (L. Hartmann & S. J. Kenyon 1996; M. Audard et al. 2014).

Young eruptive stars experience outburst events, during which their luminosity increases by up to two orders of magnitude. The outbursts are caused by a sudden increase of the mass accretion rate from the circumstellar disk onto the stellar surface, rising from 10^{-10} to $10^{-8} M_{\odot} \text{ yr}^{-1}$ in quiescence to 10^{-6} – $10^{-4} M_{\odot} \text{ yr}^{-1}$ in outburst. Recent works suggest that episodic accretion is a common process of star formation (e.g., W. J. Fischer et al. (2023) and references therein). Young eruptive stars have traditionally been classified into two main types: EX Lupi-type (EXor) objects (G. H. Herbig 2008) and FU Orionis-type (FUor) objects (G. H. Herbig 1977). Our understanding of the physics of eruptive young stars and their role in the star formation process is still incomplete. There are

several open questions, as recently reviewed by W. J. Fischer et al. (2023). What is the role of variable accretion in determining the stellar mass? Do all stars experience episodic accretion? What are the triggering mechanisms of events of episodic accretion? What physical processes lead to the end of outbursts? How can we investigate these processes based on the observed variability? What is the role of episodic accretion in the process of planet formation? To better investigate these open questions, it is important to identify new such objects as well as monitor the photometric and spectroscopic properties of the known eruptive YSOs. An opportunity to find new cases of eruptive young stars, as well as monitor the brightness of already identified targets, is provided by the Gaia Photometric Science Alerts system (S. T. Hodgkin et al. 2021) with its 4π sky coverage and approximately monthly cadence, and it has already resulted in several discoveries. Gaia17bpi (L. A. Hillenbrand et al. 2018), Gaia18dvy (E. Szegedi-Elek et al. 2020), and Gaia21elv (Z. Nagy et al. 2023) were identified as FUors, Gaia18dvz (K. W. Hodapp et al. 2019), Gaia20eae (F. Cruz-Sáenz de Miera et al. 2022; A. Ghosh et al. 2022), and Gaia19fct (S. Park et al. 2022) were identified as EXors. Some sources showed both FUor and EXor characteristics, such as Gaia19ajj (L. A. Hillenbrand et al. 2019), Gaia19bey (K. W. Hodapp et al. 2020), Gaia21bty (M. Siwak et al. 2023), and Gaia18cjb (E. Fiorellino et al. 2024). Another young star, Gaia20fgx, showed brightness variations similar to EXors, but its accretion rate turned out to be lower than the typical values for EXors (Z. Nagy et al. 2022).

Gaia23bab triggered the Gaia Alerts system on 2023 March 6 due to its 2 mag brightening. This source was previously known as a YSO candidate (G. Marton et al. 2016). The source is also known as SPICY 97589 (M. A. Kuhn et al. 2021), and was suggested to be an EXor candidate based on photometric data by M. A. Kuhn et al. (2023). Recently, T. Giannini et al. (2024) confirmed the EXor nature of the source based on spectroscopy. M. A. Kuhn et al. (2023) and T. Giannini et al. (2024) found its spectral index to be consistent with typical values of Class II sources. M. A. Kuhn et al. (2023) investigated that Gaia23bab is part of the cluster G38.3-0.9, and estimated its distance to be 900 ± 45 pc based on Gaia DR3 (Gaia Collaboration et al. 2023) parallaxes of six cluster members.

In this paper, we continue the analysis of T. Giannini et al. (2024). We provide revised stellar parameters. Based on these stellar parameters, we calculate the accretion properties at two epochs during the 2023 outburst. We probe the excitation conditions traced by the H I lines at three epochs, and discuss the detections of other species such as Ca II, He I, and O I. We discuss the photometric and spectroscopic data used in this paper in Section 2, present results on revised stellar parameters, color variations, line detections, accretion rates, H I excitation, and physical properties probed by the Ca II, He I, and O I lines in Section 3, discuss them in Section 4, and summarize them in Section 5.

2. Observations

2.1. Photometry

We obtained optical photometric observations of Gaia23bab with the 80 cm Ritchey–Chrétien telescope (RC80) at the Pizskéstető Mountain Station of Konkoly Observatory (Hungary). The RC80 telescope was equipped with an FLI PL230 CCD camera, $0''.55$ pixel scale, $18''.8 \times 18''.8$ field of view

(FoV), Johnson *BV* and Sloan *g'r'i'* filters. We typically obtained three images in each filter. We first applied CCD reduction, including bias, flat-field, and dark current corrections. Then we performed aperture photometry for the science target and several comparison stars in the FoV using an aperture radius of $2''.75$. We selected those comparison stars from the APASS9 catalog (A. A. Henden et al. 2015) that were within $6''.5$ of the target and which were mostly constant, i.e., the rms of their *V*-band observations from the ASAS-SN Photometry Database (B. J. Shappee et al. 2014; T. Jayasinghe et al. 2019) were below 0.1 mag. The APASS9 catalog provided Bessell *BV* and Sloan *g'r'i'* magnitudes for the comparison stars. We used the comparison stars for the photometric calibration by fitting a linear color term. Magnitudes taken with the same filter on the same night were averaged. The final uncertainties are the quadratic sum of the formal uncertainties of the aperture photometry, the photometric calibration, and the scatter of the individual magnitudes that were averaged per night. The results can be found in Appendix A.

Observations were performed with the 60 cm Carl Zeiss telescope at Mount Suhora Observatory of the Cracow Pedagogical University (Poland). The telescope at Mount Suhora was equipped with an Apogee Aspen-47 camera, $1''.116$ pixel scale, $19''.0 \times 19''.0$ FoV, and Johnson *BVRI* filters. After standard reduction steps on bias, dark, and flat-field, these observations were uploaded to the BHTOM service,¹⁹ where they were converted to standard magnitudes. The results are shown in Appendix A.

We used the NOTCam instrument on the Nordic Optical Telescope (NOT) on 2023 March 14 and 15 to obtain near-infrared (NIR) photometry (Program ID: 66-109; PI: F. Cruz-Sáenz de Miera). The instrument includes a 1024×1024 pixel HgCdTe Rockwell Science Center “HAWAII” array, and for wide-field imaging, it has a $4' \times 4'$ FoV (pixel scale: $0''.234$). We obtained five images in each of the *JHK_s* bands with 4 s exposures. The data were reduced using our own IDL routines. Data reduction steps included sky subtraction, flat-fielding, and coadding exposures by dither position and filter. To calibrate the photometry, we used the Two Micron All Sky Survey (2MASS) catalog (R. M. Cutri et al. 2003). The instrumental magnitudes of the target and all good-quality 2MASS stars in the field were extracted using an aperture radius of $2''$ in all filters. We determined a constant offset between the instrumental and the 2MASS magnitudes by averaging typically 20–30 stars. The resulting magnitudes are $J = 13.560 \pm 0.022$ mag, $H = 12.382 \pm 0.013$ mag, and $K_s = 11.583 \pm 0.022$ mag.

We also took *JHK_s* images of Gaia23bab with the infrared guiding camera of SpeX, a medium-resolution infrared spectrograph (J. T. Rayner et al. 2003) on the NASA Infrared Telescope Facility (IRTF) on Maunakea, Hawai'i (USA) on 2023 September 1 (Program ID: 2023B037; PI: á. Kóspál) using a 5-point dither pattern and 5 s exposures. We used the dithering to make a sky image, which we subtracted from the shifted and coadded images. Finally, we obtained aperture photometry for Gaia23bab and several other stars in the approximately $1' \times 1'$ FoV as comparison stars. We used 2MASS for the photometric calibration. The resulting magnitudes are $J = 13.546 \pm 0.056$ mag, $H = 12.443 \pm 0.097$ mag, and $K_s = 11.593 \pm 0.095$ mag.

¹⁹ BHTOM—Black Hole TOM: <https://bhtom.space>.

Table 1

Characteristic Timescales and Amplitudes of the Outbursts in Different Bands Obtained Using a Gaussian Fitting

Outburst, Band	Amplitude (mag)	Center (MJD 57000)	FWHM (days)
2017 WISE W1	1.1 ± 0.1	962 ± 16	244 ± 37
2017 WISE W2	1.3 ± 0.1	976 ± 12	267 ± 24
2017 Gaia <i>G</i>	2.3 ± 0.2	968 ± 10	175 ± 12
2023 WISE W1	1.6 ± 0.2	2970 ± 50	400 ± 60
2023 WISE W2	1.7 ± 0.2	2970 ± 50	380 ± 60
2023 Gaia <i>G</i>	2.3 ± 0.1	2996 ± 10	337 ± 17
2023 ZTF <i>r</i>	2.7 ± 0.3	3005 ± 45	330 ± 25

In addition to our own photometry, we used archival optical and infrared photometry. We used mid-infrared photometry from the Wide-field Infrared Survey Explorer (WISE; E. L. Wright et al. 2010) and NEOWISE (A. Mainzer et al. 2011) surveys from the NASA/IPAC Infrared Science Archive. NEOWISE observed the full sky on average twice per year with multiple exposures per epoch. For a comparison with the photometry from other instruments, we computed the average of multiple exposures of each season. We derived the average of the uncertainties of the single exposures (err1). We also calculated the standard deviation of the points we averaged per season (err2). For the error of the data points averaged per epoch, we used the maximum of err1 and err2.

We downloaded *G*-band photometry from the Gaia Science Alerts Index website. We used *r*- and *g*-band photometry from Data Release 21 of the Zwicky Transient Facility (ZTF; F. J. Masci et al. 2019). We ignore the data points that have $\text{catflag} = 32768$, as these are likely affected by clouds and/or the Moon. We also downloaded *o*- (“orange,” 560–820 nm) and *c*- (“cyan,” 420–650 nm) band magnitudes from the Asteroid Terrestrial-impact Last Alert System (ATLAS; A. N. Heinze et al. 2018; J. L. Tonry et al. 2018; K. W. Smith et al. 2020) survey using the ATLAS Forced Photometry web service (L. Shingles et al. 2021). Data points fainter than 20 mag were not considered in our analysis, given the ATLAS limiting magnitude of ~ 20 mag (J. L. Tonry et al. 2018).

2.2. Spectroscopy

We used the NOT/NOTCam to obtain intermediate-resolution ($R = 2500$) *JHK* spectra on 2023 March 14/15 (Program ID: 66-109; PI: F. Cruz-Sáenz de Miera). We used the ABBA nodding pattern along the slit. The exposure time was 1176 s in each band. The nearby telluric standard star HIP 86349 was observed right before the target observation for telluric correction. The raw data were reduced using IRAF (D. Tody 1986) for sky subtraction, flat-fielding, bad-pixel removal, aperture tracing, and wavelength calibration. Argon and xenon lamp spectra were used for the wavelength calibration. Hydrogen lines in the spectra of the telluric standard were removed, and then the spectra were normalized. The target spectrum was divided by the normalized telluric spectrum to correct for the telluric lines.

We obtained another NIR spectrum of Gaia23bab using IRTF/SpEX (J. T. Rayner et al. 2003) on 2023 September 1 (Program ID: 2023B037; PI: Á. Kóspál). We utilized the short-wavelength cross-dispersed grating with the $0.8 \times 15''$ slit, covering the 0.69–2.57 μm wavelength range with a spectral

resolution of $R = 800$. The total integration time was 2160 s, split into several exposures to avoid saturation and to enable proper sky subtraction and cosmic hit rejection. For telluric correction, we observed the A0-type star 5 Vul using the same instrument setup and at the same airmass (1.04) as the science target, with a total integration time of 720 s. We reduced the data using Spextool (W. D. Vacca et al. 2003; M. C. Cushing et al. 2004). Reduction steps included flat-field correction, wavelength calibration using argon arc spectra, the subtraction of the images taken at the A and B nod positions along the slit for sky subtraction, calculation of a spatial profile along the slit length, the extraction of the 1D spectra in an aperture positioned at the peak of the spatial profile, the combination of the individual exposures, telluric correction, and flux calibration, and the merging of the individual orders. Contemporaneous photometric observations were used for flux calibration.

3. Results

3.1. Light and Color Variations

The top panel of Figure 1 shows the Gaia *G*, (NEO)WISE, and ATLAS light curve of Gaia23bab. In addition to the 2023 outburst, an earlier outburst in 2017 is also seen in the light curve with a duration of about 1 yr (M. A. Kuhn et al. 2023; T. Giannini et al. 2024). The amplitude (~ 2 mag in the Gaia *G* band) is similar for both outbursts. The bottom panel of Figure 1 includes the ZTF photometry and the data obtained after the Gaia alert using the Piszkestető RC80 telescope. Based on the ATLAS and the Piszkestető RC80 photometry, Gaia23bab finished its outburst and is back in quiescence. To quantitatively compare the two outbursts, we fitted Gaussians in different bands: in WISE W1, W2, and Gaia *G* for the 2017 outburst, and additionally in ZTF *r* for the 2023 outburst. The results of the Gaussian fitting are shown in Table 1 and the fitted Gaussians are shown in Figure 1. The duration of the 2023 outburst is longer than that of the 2017 outburst. The amplitude of the outbursts is similar in Gaia *G*, but larger for the 2023 outburst in the WISE bands. The duration of both outbursts is longer based on the WISE light curves than in the optical, based on Gaia and ZTF. However, the cadence of the WISE light curve is lower than that of the optical light curves.

Figure 2 shows the $[g - r]$ versus *g* color–magnitude diagram based on the ZTF data, which mostly corresponds to the brightening phase of the 2023 outburst. These data show that the color of the brightening is mostly gray. The $[r - i]$ versus *r* color–magnitude diagram based on photometry obtained with the Piszkestető RC80 telescope as well as the $[R - I]$ versus *V* and $[V - R]$ versus *V* color–magnitude diagrams based on Mt. Suhora data (Figure 2) during the maximum and the fading phase of the outburst show color variations related to changes in the extinction.

Photometry from the ATLAS survey is available during both outbursts, which allows a comparison of the color evolution of the 2017 and 2023 outbursts (Figure 3). For a comparison of the *o* and *c* magnitudes, we interpolated the light curves at the same epochs, and averaged the data points in 3 day bins. As seen in Figure 3, both color–magnitude diagrams show color variations which may be partly related to variable circumstellar extinction. Therefore, in addition to the similar amplitude and duration, both outbursts show similar

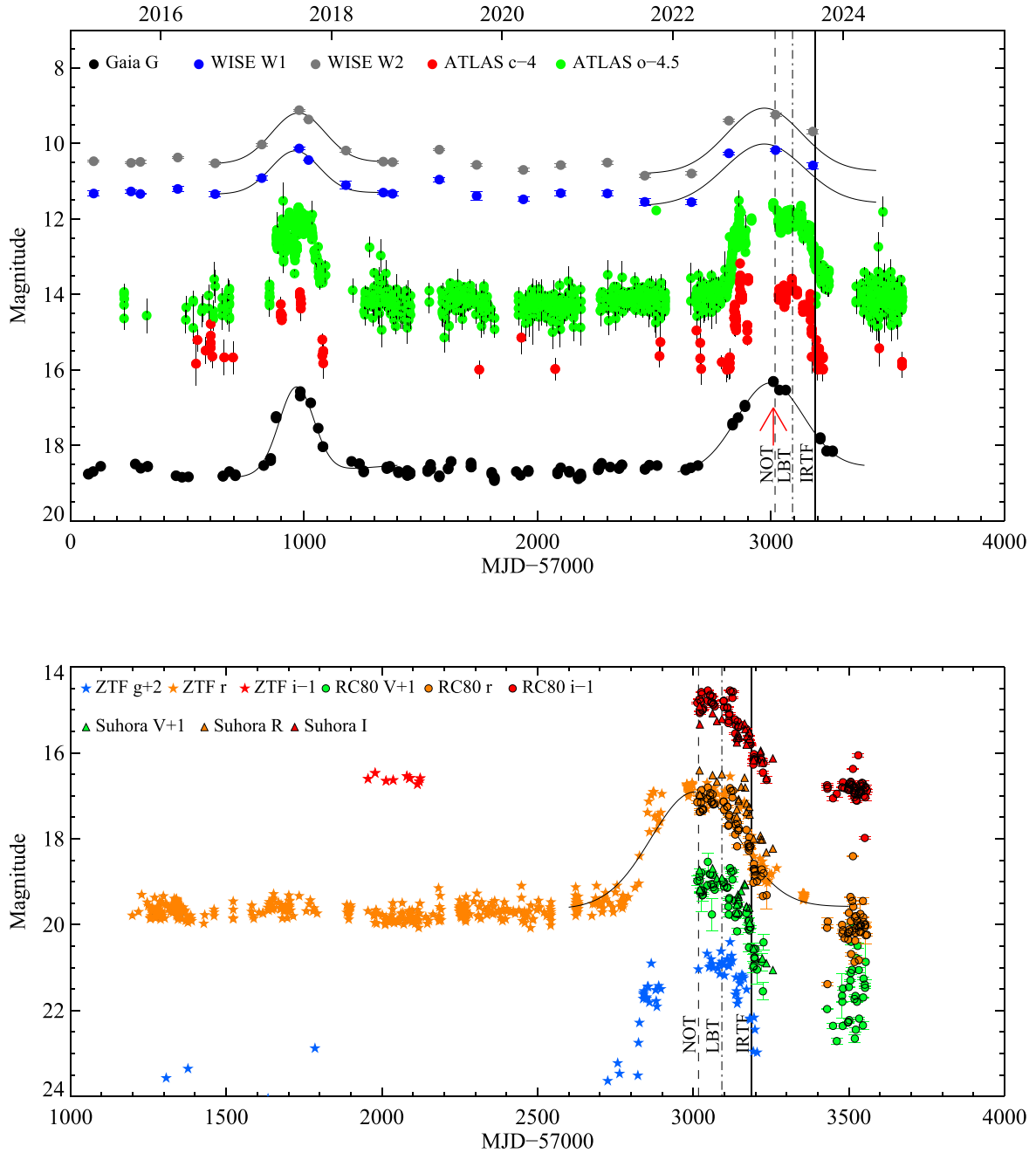


Figure 1. Top panel: Gaia G , WISE, and ATLAS light curve of Gaia23bab. The red arrow shows the date of the Gaia alert. The lines show the epochs of the NOT, LBT, and IRTF spectra. Bottom panel: ZTF, Piszkestető RC80, and Mt. Suhora light curve of Gaia23bab. Gaussians fitted to the outbursts are shown in both light curves.

color variations, as was also suggested by $[r - i]$ versus $[g - r]$ color-color diagrams investigated by T. Giannini et al. (2024).

Figure 4 shows a color-magnitude diagram based on the WISE W1 and W2 bands. The source is generally redder when brighter, which is the opposite of what we expect from extinction-related variability, which would cause redder colors when the source is fainter, as also suggested by T. Giannini et al. (2024). Since the W1 and W2 fluxes originate from the inner regions of the disk, this variability indicates the variations of these disk regions. The areas of the inner-disk regions may have increased due to the outburst.

Figure 5 shows the $[J - H]$ versus $[H - K_S]$ color-color diagrams based on 2MASS photometry, Large Binocular Telescope (LBT) photometry from T. Giannini et al. (2024) obtained during the 2023 outburst, the data point obtained with the NOT around the brightest state of the 2023 outburst, and the IRTF data point obtained during the fading phase of the 2023 outburst. For a comparison, we plotted the $[J - H]$ and $[H - K_S]$ colors for the EXor sample of D. Lorenzetti et al. (2009), except for PV Cep, as its $[J - H]$ and $[H - K_S]$ values are outside of the plotted range due to very high extinction. The $[J - H]$ versus $[H - K_S]$ colors of Gaia23bab at the different epochs are consistent with those of the sample of EXors.

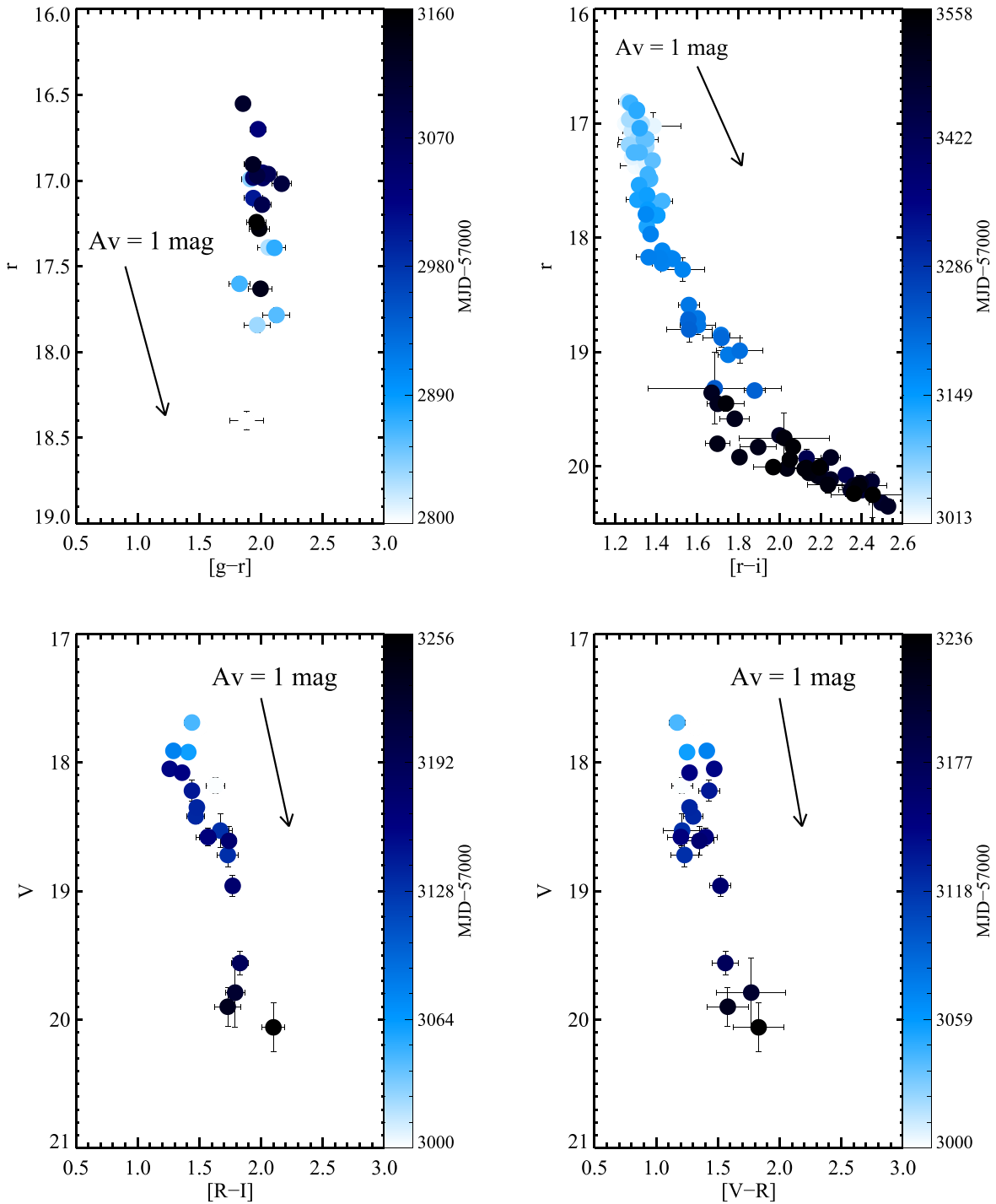


Figure 2. Top left panel: color–magnitude diagram based on ZTF g and r magnitudes, mostly during the brightening phase of the 2023 outburst. Top right panel: color–magnitude diagram during the fading phase of the outburst based on follow-up photometry using the Piszkestető RC80 telescope. Bottom panels: V vs. $[R - I]$ and V vs. $[V - R]$ color–magnitude diagrams based on Mt. Suhora photometry covering mostly the fading phase.

3.2. Line Detections

The first spectrum observed with the NOT was taken on 2023 March 14/15, soon after the Gaia alert was issued on 2023 March 6, close to the maximum brightness of the source. The second spectrum observed on 2023 September 1 with the IRTF was obtained during the fading of the source. Therefore, these spectra represent two different phases of the outburst. For comparison, we include in our analysis the spectrum of T. Giannini et al. (2024) obtained with the LBT between the

NOT and IRTF epochs, on 2023 May 28/29, when the source was already fading. Figure 6 shows the NOT, LBT, and IRTF spectra and a spectrum of EX Lupi from Á. Kóspál et al. (2011)—the prototype of EXors—during outburst. The lines identified in the spectra are shown in Appendix B, and their equivalent widths are shown in Appendix B. The profiles of the hydrogen lines are shown in Appendix B. The IRTF spectrum has the widest wavelength coverage as seen in Figure 6; however, as it was already taken during the fading

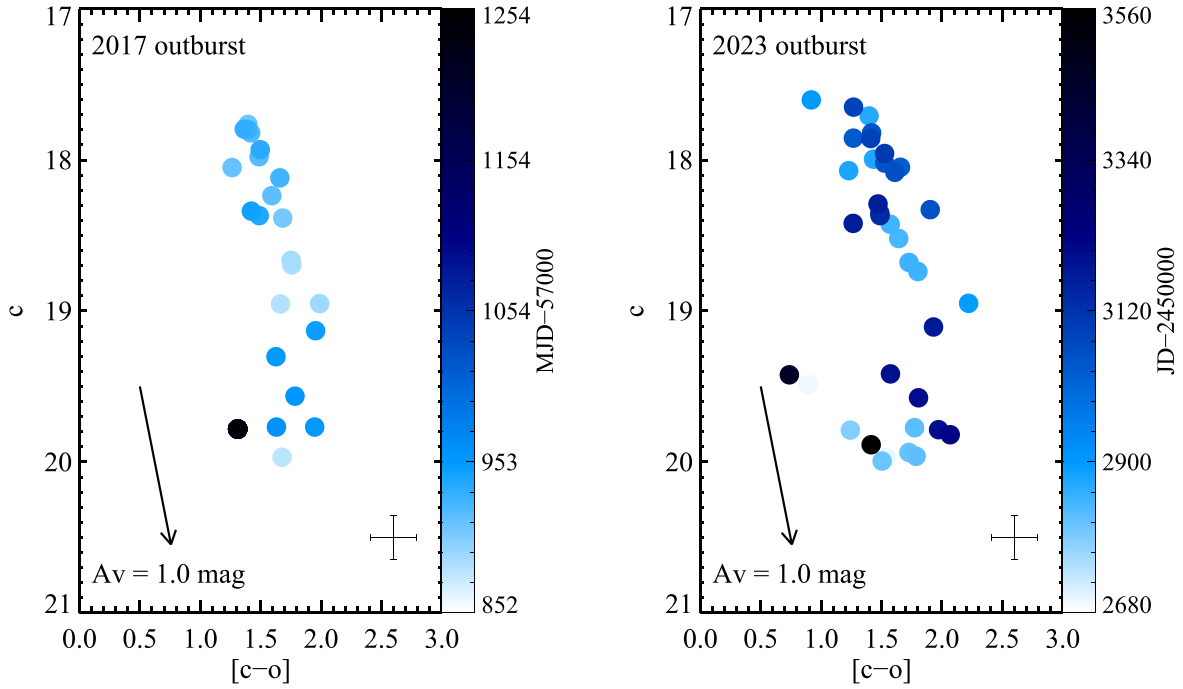


Figure 3. Color–magnitude diagrams during the 2017 (left panel) and 2023 (right panel) outbursts based on o and c magnitudes from the ATLAS survey. The typical error of the data points is plotted in the lower right corner of the figures.

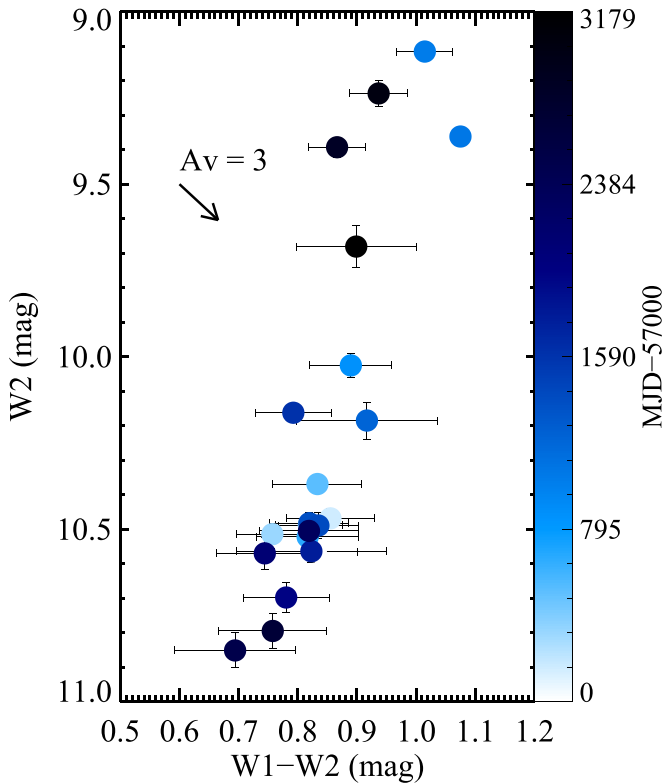


Figure 4. Color–magnitude diagram based on WISE W1 and W2 data, covering both the 2017 and 2023 outbursts.

phase, there are some lines that were detected at the earlier epochs, but not in the IRTF spectrum, such as the CO bandhead. The NaI doublet lines at $2.2 \mu\text{m}$, which are also tracing the disk, are only tentatively detected in the IRTF spectrum, while they are clearly seen at the earlier epochs.

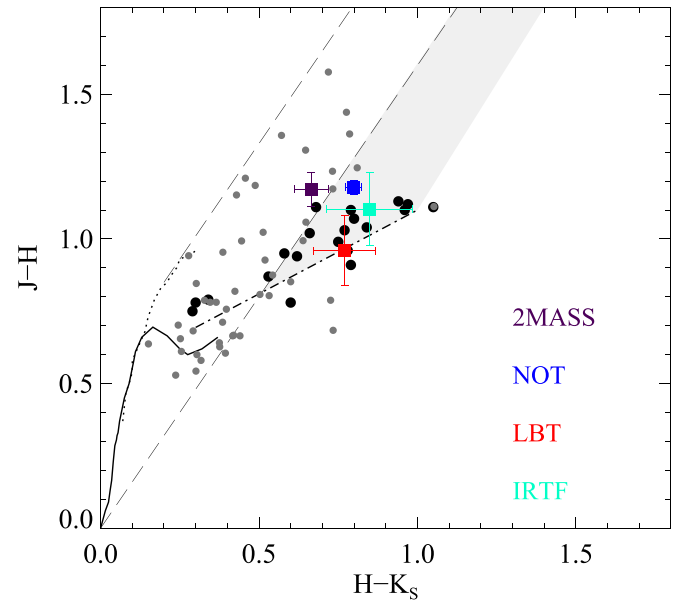


Figure 5. $(J - H)$ vs. $(H - K_s)$ color–color diagram. The solid curve shows the colors of the zero-age main-sequence, and the dotted line represents the giant branch (M. S. Bessell & J. M. Brett 1988). The long-dashed lines delimit the area occupied by the reddened normal stars (J. A. Cardelli et al. 1989). The dashed–dotted line is the locus of unreddened CTTS (M. R. Meyer et al. 1997) and the gray shaded band borders the area of the reddened K_s -excess stars. The black dots correspond to the EXor sample from D. Lorenzetti et al. (2009), the smaller gray dots correspond to the young stellar cluster NGC 7023 from M. Szilágyi et al. (2021).

Several accretion tracers are detected, such as the Ca II triplet, He I, and hydrogen lines from the Paschen series covered by the LBT and IRTF spectra, and from the Brackett series detected at each epoch from Br20 to Br γ , with the exception of the Br9 and Br δ lines, which are only covered by the IRTF spectrum. Several metallic lines were detected at each epoch,

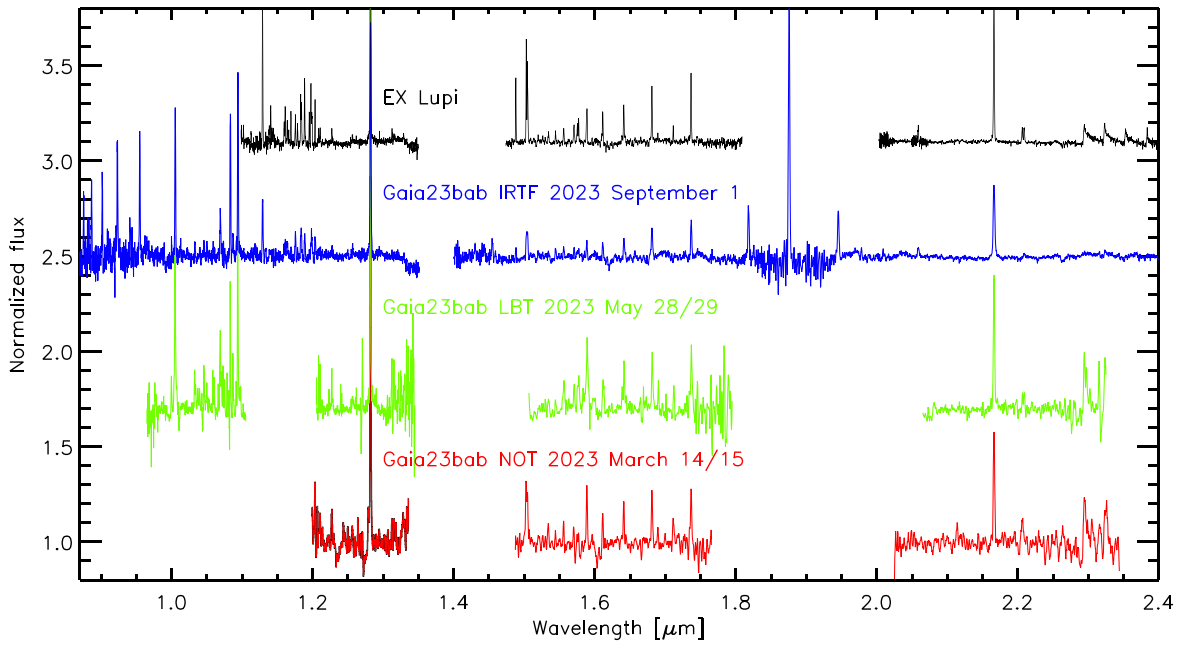


Figure 6. Comparison of the NOT, LBT, and IRTF spectra of Gaia23bab with that of EX Lupi from Á. Kóspál et al. (2011).

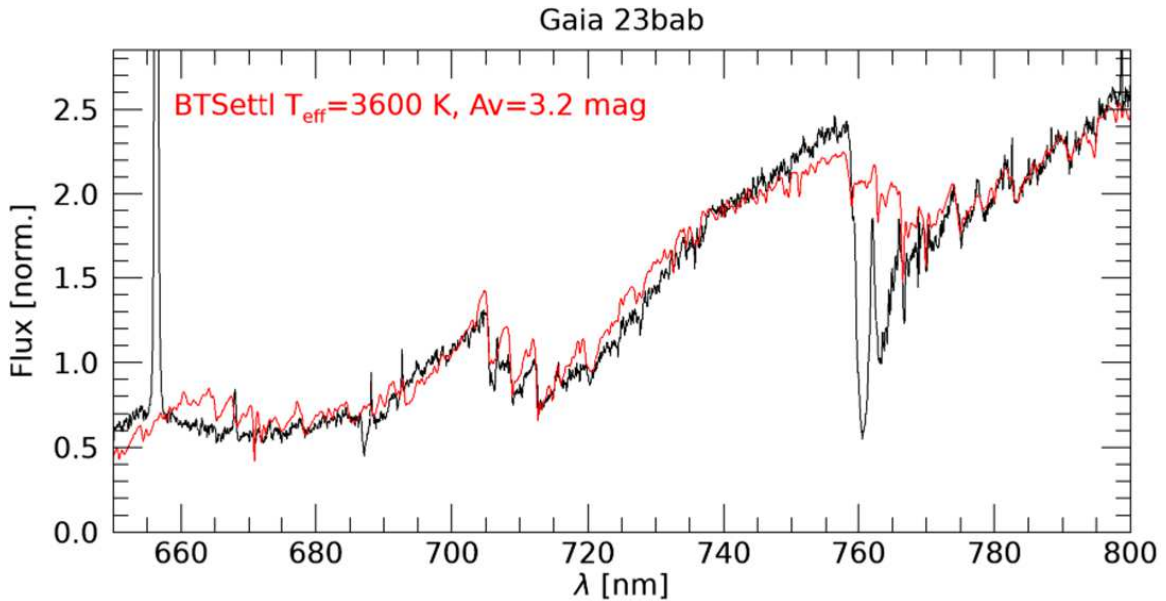


Figure 7. Part of the Gaia23bab spectrum obtained with the LBT in quiescence and the best-fitting photospheric template.

such as those of Na, Mg, Fe, Si, Ca, Al, C, and O. The [Fe II] line at $1.644 \mu\text{m}$, a shock-excited line, is detected at each epoch; however, it is blended with the Br12 line. T. Giannini et al. (2024) report the weak detection of another shock tracer, the H_2 line at $2.1218 \mu\text{m}$, but it is not detected at the other two epochs.

3.3. Revised Stellar Parameters

In T. Giannini et al. (2024), an estimate of the stellar parameters was obtained based on the extinction and NIR 2MASS photometry in the quiescent phase. On 2024 April 11, a quiescence spectrum of Gaia23bab was obtained with the two spectrographs MODS (optical) and LUCI (NIR) mounted on the 8.4 m LBT (Arizona, USA). This spectrum will be presented in a forthcoming paper, and here we report the analysis of the

optical continuum used to determine the spectral type of Gaia23bab (Figure 7). The spectrum presents the TiO molecular bands at $\sim 720 \text{ nm}$, which can be fitted with an M1 stellar template. In addition, the spectral slope is fitted by assuming $A_V = 3.2 \pm 0.5 \text{ mag}$. Knowing the spectral type, we can then estimate the stellar luminosity from the observed magnitudes corrected for the extinction and assuming a bolometric correction (BC). We used the value $BC_J = 1.74$ in the J band estimated for 5–30 Myr stars by M. J. Pecaut & E. E. Mamajek (2013). From the same paper, we also took the effective temperature ($T_{\text{eff}} = 3630 \text{ K}$) corresponding to M1 stars. The stellar luminosity (L_*) is then computed as $\log(L_*/L_\odot) = 0.4 (M_{\text{bol},\odot} - M_{\text{bol}})$, where $M_{\text{bol},\odot} = 4.74$ (E. E. Mamajek et al. 2015) and M_{bol} is the intrinsic bolometric magnitude, $M_{\text{bol}} = m_J - 5 \log(d/10(\text{pc})) + BC_J = 5.08$. This results in

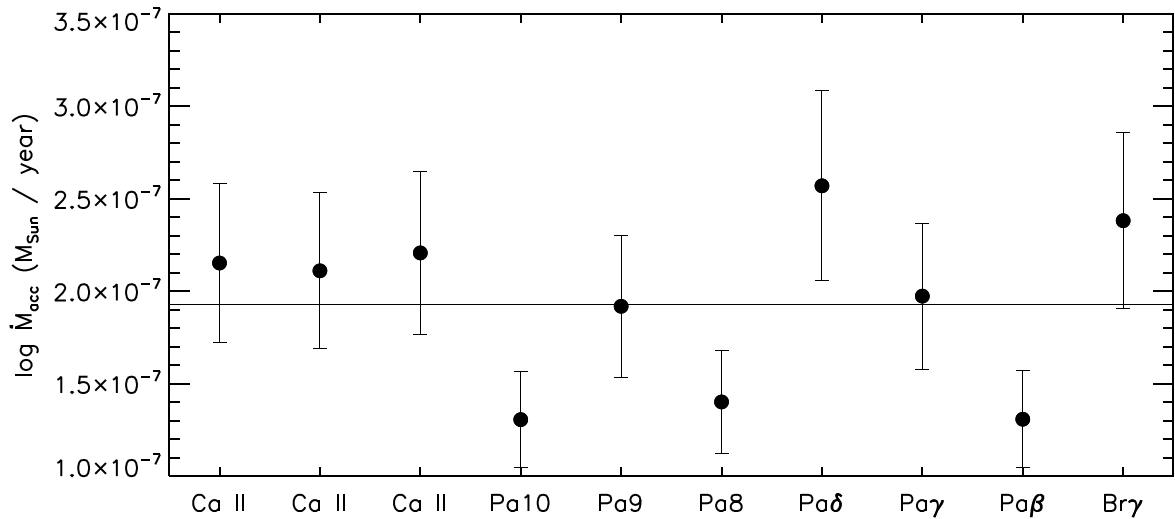


Figure 8. The accretion rates derived based on the accretion tracers detected in the IRTF spectrum when assuming an A_V of 3.6 mag and stellar parameters derived in Section 3.3.

Table 2

Fluxes of the Lines (Not Corrected for Extinction), Which are Used to Estimate the Accretion Parameters from the NOT and IRTF Spectra

Species	λ_{tab} (μm)	$F(\text{NOT})$ ($10^{-15} \text{ erg s}^{-1} \text{ cm}^{-2}$)	$F(\text{IRTF})$
Ca II	0.8498	...	33.6 ± 5.0
Ca II	0.8542	...	37.8 ± 5.7
Ca II	0.8662	...	35.0 ± 5.3
H I (Pa10)	0.9015	...	3.8 ± 0.6
H I (Pa9)	0.9229	...	5.5 ± 0.8
H I (Pa8)	0.9546	...	7.3 ± 1.1
H I (Pa δ)	1.0049	...	10.2 ± 1.5
He I	1.0830	...	10.7 ± 1.6
H I (Pa γ)	1.0938	...	14.7 ± 2.2
H I (Pa β)	1.2821	36.0 ± 5.4	24.5 ± 3.7
H I (Br γ)	2.1661	15.4 ± 2.3	12.0 ± 1.8

$L_* = 0.72 \pm 0.07 L_\odot$. Then, the stellar radius is derived from L_* and T_{eff} , assuming that the source emits as a blackbody. We estimate $R_* = 2.3 \pm 0.2 R_\odot$. Finally, mass is derived from the evolutionary tracks of L. Siess et al. (2000) as $M_* = 0.40 \pm 0.05 M_\odot$.

3.4. Accretion Parameters

In the following section, we derive the accretion rates based on several accretion tracers observed in the NOT and IRTF spectra. The line fluxes shown in Table 2 can be converted to line luminosities after extinction correction as $L_{\text{line}} = 4\pi d^2 f_{\text{line}}$, where d is the distance to the source, and f_{line} is the extinction-corrected flux of the lines. We assume the distance of 900 ± 45 pc estimated by M. A. Kuhn et al. (2023). For the IRTF epoch, we considered different A_V values, as the accretion rates derived from the different lines are supposed to be the same for the right A_V . There are only two accretion tracers at the NOT epoch; therefore, we assume an A_V of 3.2 ± 0.5 mag for this epoch, as was derived in Section 3.3. We convert the line luminosities to accretion luminosities using the relations derived by J. M. Alcalá et al. (2017). The accretion luminosities can then be converted to accretion rates

using the formula

$$\dot{M}_{\text{acc}} = 1.25 \frac{L_{\text{acc}} R_*}{GM_*} \quad (1)$$

for which an inner-disk radius of $5 R_*$ was assumed (L. Hartmann et al. 1998). We assume the stellar radius and mass derived in Section 3.3. We derive an accretion luminosity of $0.9 \pm 0.2 L_\odot$ and an accretion rate of $(2.0 \pm 0.5) \times 10^{-7} M_\odot \text{ yr}^{-1}$ for a best-fitting A_V of 3.6 mag at the epoch of the IRTF spectrum. This value is the average value based on all the accretion tracers observed in the IRTF spectrum, as shown in Figure 8, and its error is the standard deviation. At the epoch of the NOT spectrum, only the Pa β and Br γ lines are available to measure the accretion luminosity and rate, which are $\sim 0.8 L_\odot$ and $\sim 1.4 L_\odot$ and $1.9 \sim 10^{-7} M_\odot \text{ yr}^{-1}$ and $3.2 \sim 10^{-7} M_\odot \text{ yr}^{-1}$, respectively. The accretion rates estimated at the NOT and IRTF epochs are similar to the value of $(2.5 \pm 0.6) \times 10^{-7} M_\odot \text{ yr}^{-1}$ derived by T. Giannini et al. (2024) for the epoch of the LBT spectrum, and imply that the accretion rate did not change significantly during the outburst.

3.5. Hydrogen Lines

Strengths of the hydrogen lines provide information about the physical conditions—temperatures and densities—of the emitting medium. In the following, we compare the observed Brackett, Paschen, and Balmer decrements to model predictions. We use extinction-corrected fluxes, for which we assume an A_V of 3.6 ± 0.4 mag, which is based on the accretion rate estimate at the IRTF epoch and the assumption that the A_V did not change significantly between the epochs, which is consistent with the result of the fitting by a stellar template in Section 3.3.

3.5.1. Brackett Decrements

To estimate excitation conditions based on the line strengths of the Brackett series, we compare the observed values to the predictions of Case B theory (D. G. Hummer & P. J. Storey 1987). Case B theory assumes that the emitting plasma is opaque to Ly α photons and optically thin for higher transition lines. The

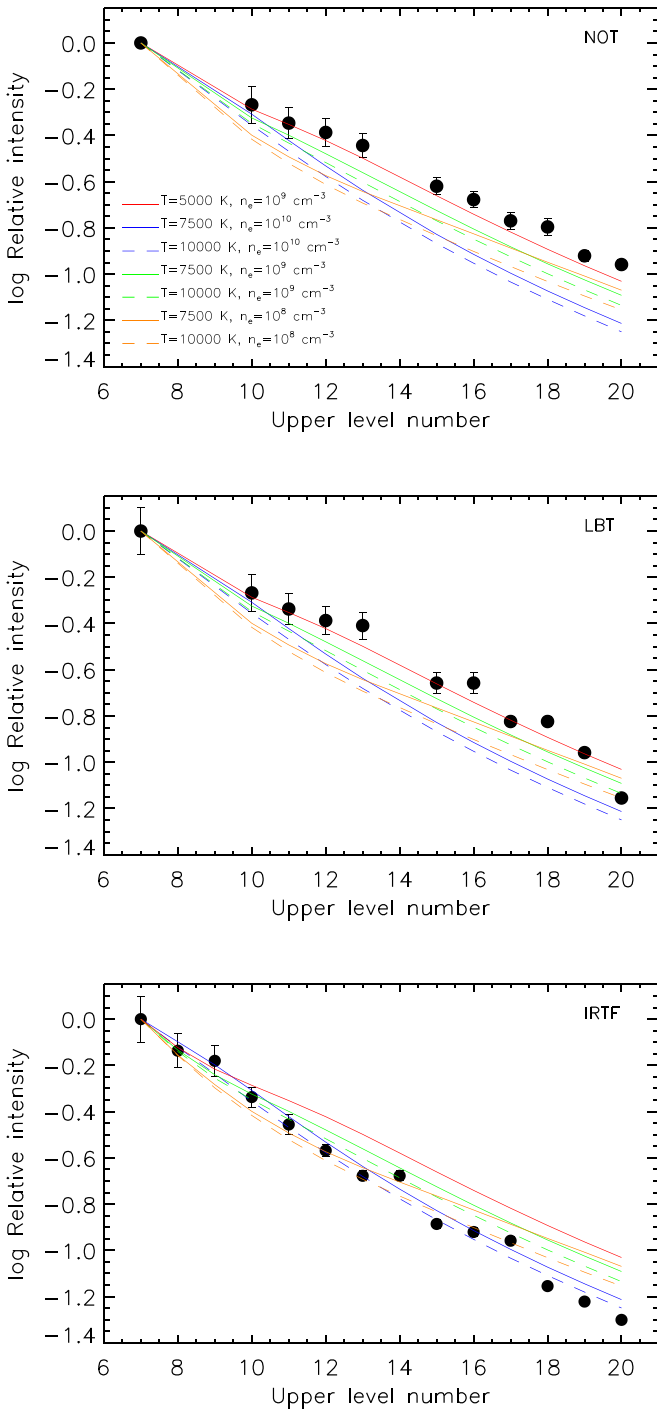


Figure 9. Excitation diagrams for the hydrogen Brackett series for the NOT, LBT, and IRTF spectra. The fluxes have been normalized by the flux of the Br γ line. The red line shows the best-fitting model at the NOT and LBT epochs, and the blue lines show the best-fitting models at the IRTF epoch.

D. G. Hummer & P. J. Storey (1987) models are available for electron densities of 10^2 , 10^3 , 10^4 , 10^5 , 10^6 , 10^7 , 10^8 , 10^9 , and 10^{10} cm^{-3} and for temperatures of 1000, 3000, 5000, 7500, 10,000, and 12,500 K. To find the best-fitting model(s) at the three epochs, we applied χ^2 minimization. The results for the three epochs are shown in Figure 9. The best-fit temperature is 5000 K and the best-fit electron density is 10^9 cm^{-3} at the NOT and LBT epochs. The flux ratios at the IRTF epoch can be better fitted with an electron density of 10^{10} cm^{-3} , and are consistent with temperatures of 7500

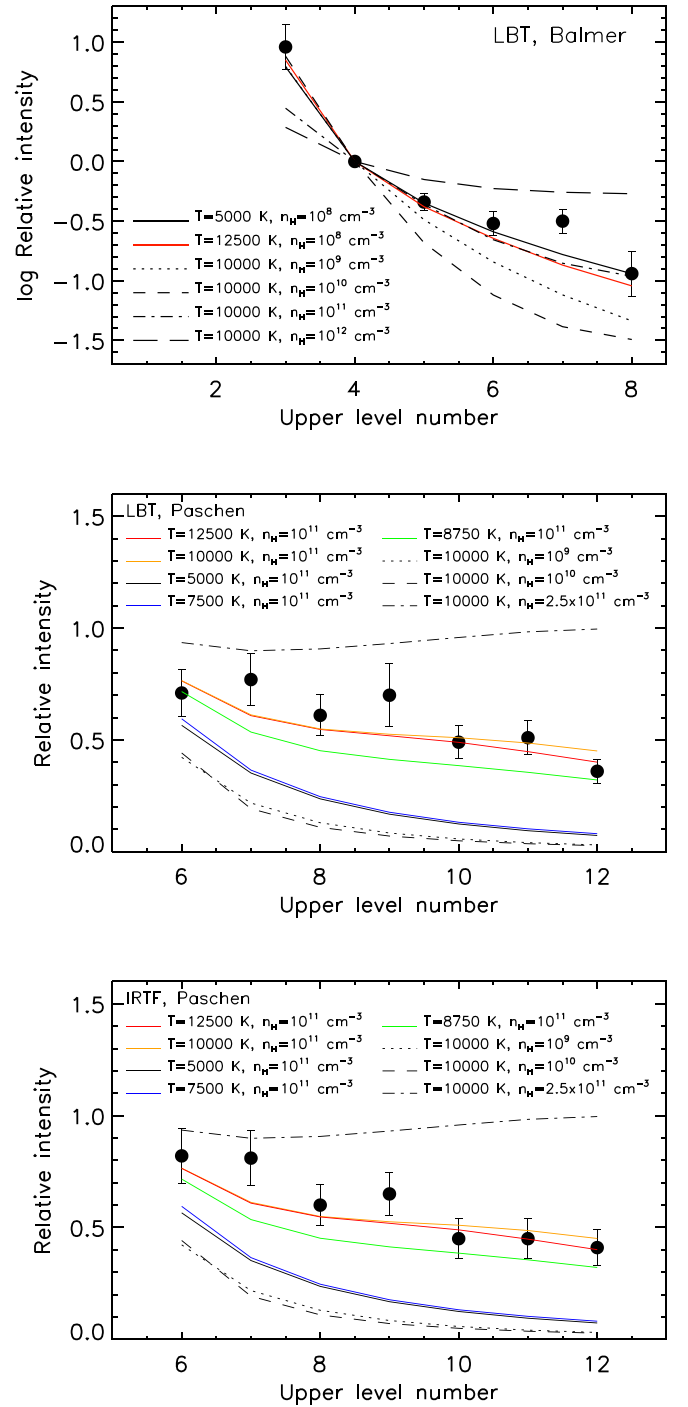


Figure 10. Excitation diagrams for the hydrogen Balmer series normalized to the flux of the H β line based on the LBT spectrum (top), and the Paschen series normalized to the flux of the Pa β line based on the LBT (middle) and IRTF during the outburst (bottom) spectra. The overlotted lines correspond to model predictions from J. Kwan & W. Fischer (2011) and S. Edwards et al. (2013).

and 10,000 K. The best-fit parameters at the NOT and LBT epochs are similar to those found using the same method for the eruptive young star V899 Mon (S. Park et al. 2021). The results for each epoch for Gaia23bab differ from the results of Á. Kóspál et al. (2011) for EX Lupi, who found a best-fit temperature of 10,000 K and an electron density of 10^7 cm^{-3} . However, Case B theory has been applied to investigate the excitation conditions of several

other YSOs (e.g., B. Nisini et al. 2004; J. S. Bary et al. 2008; L. Podio et al. 2008; W. D. Vacca & G. Sandell 2011; S. Kraus et al. 2012; E. T. Whelan et al. 2014), and the estimated temperatures and densities both span a huge range, with values of $T = 1000\text{--}20,000$ K and electron densities in the range between 10^7 and 10^{13} cm^{-3} . Due to the large range of best-fit parameters and the assumptions of the method, the validity of Case B theory for circumstellar environments of T Tauri stars has been questioned (S. Edwards et al. 2013).

3.5.2. Balmer and Paschen Decrements

Local line excitation calculations have been developed by J. Kwan & W. Fischer (2011) for conditions appropriate for winds and accretion flows of T Tauri stars. These calculations give predictions for the Balmer and Paschen series. Predictions for the Balmer decrements (ratios from H15 to H α with respect to H β) in the model are given for densities $8 < \log(n_{\text{H}})$ (cm^{-3}) < 12.4 and temperatures between 3750 and 15,000 K. Predictions for the Paschen decrements by S. Edwards et al. (2013; ratios from Pa γ to Pa12 with respect to Pa β) are available for a range of densities ($8 < \log(n_{\text{H}})$ (cm^{-3}) < 12.4) and temperatures (5000–20,000 K). The Paschen decrements for Gaia23bab are covered by the LBT and IRTF spectra, while the Balmer decrement is covered by the LBT spectrum.

Fluxes of the Balmer series are most consistent with a density of $n_{\text{H}} = 10^8$ cm^{-3} . For this density, models with temperatures between 3750 and 12,500 K can reproduce the observed flux ratios. A temperature of 3750 K is unlikely since it is below the stellar temperature (see Section 3.3); therefore, the range of temperatures consistent with the Balmer decrement is likely to be between 5000 and 12,500 K. Figure 10 shows models with $n_{\text{H}} = 10^8$ cm^{-3} and 5000 K as well as 12,500 K. It also demonstrates, that the observed flux ratios cannot be fitted with any other H density.

At both epochs, the fluxes of the Paschen series are closest to the predictions of a model with $T = 10,000$ K and $n_{\text{H}} = 10^{11}$ cm^{-3} as well as to a model with $T = 12,500$ K and $n_{\text{H}} = 10^{11}$ cm^{-3} (Figure 10). As a comparison, we plotted other models with different temperatures and densities. A model with the same temperature (10,000 K) and a density of 10^{12} cm^{-3} is outside of the plotted ranges.

The large range of temperatures found to be consistent with the fluxes of the Balmer series for Gaia23bab is similar to those derived for the sample of EXors studied by T. Giannini et al. (2022); however, the best-fit density is lower than those found for that EXor sample. The best-fit density of $n_{\text{H}} = 10^{11}$ cm^{-3} found for the Paschen series for Gaia23bab was only found in a few cases in the sample of T. Giannini et al. (2022), such as PV Cep, DR Tau, and iPTF15afq. The densities and temperatures found from the Balmer and Paschen decrements for Gaia23bab are similar to those measured for other EXors. The best-fit temperatures are consistent with the range that can be expected for H I emission in accretion columns ($T = 6000\text{--}20,000$ K; e.g., S. C. Martin 1996; J. Muzerolle et al. 2001).

3.6. Ca II, He I, and O I Lines

The Ca II triplet, the He I, and O I lines are also related to the accretion process, but may trace different regions of the accretion flow compared to the H I lines. Certain ratios of these lines may include additional information on excitation conditions in Gaia23bab. Based on the data presented here,

we analyze the Pa γ /10830 He I ratio as well as the Ca II 8498/O I 8446 and the Ca II 8498/Pa γ ratios and compare them to predictions of the J. Kwan & W. Fischer (2011) models.

The 10830 He I line, which is observed in the LBT and IRTF spectra, is the only allowed radiative transition following the 5876 He I transition. The comparison of the 10830 He I line to Pa γ is straightforward due to the proximity of their wavelengths, as well as due to their density dependence shown in J. Kwan & W. Fischer (2011) in their Figure 8. The Pa γ /He I ratio is ~ 1.9 at the LBT epoch and ~ 1.4 at the IRTF epoch. Based on Figure 8 of J. Kwan & W. Fischer (2011), these line ratios are mostly consistent with H densities between 10^{10} and 10^{11} cm^{-3} . The change in the Pa γ /He I ratio between the LBT and IRTF epochs could result from decreased optical depth (see Figure 8 in J. Kwan & W. Fischer 2011). Pa γ /He I 10830 ratios > 1 are not typical of classical T Tauri stars (CTTS; e.g., Figure 10 in J. Kwan & W. Fischer 2011). The Pa γ /He I 10830 ratio was also found to be below 1 for another EXor, V1741 Sgr (M. A. Kuhn et al. 2024).

We can compare the Ca II triplet lines to Pa γ , as it is a strong hydrogen line not far in wavelength, and to O I 8446 due to its proximity in wavelength as well as its relation to hydrogen excitation via Ly β fluorescence. The Ca II 8498/O I 8446 as well as the Ca II 8498/Pa γ line ratios have similar dependencies on $N(\text{H})$ and T and have been found to belong to two main groups (J. Kwan & W. Fischer 2011): for one of these groups, the Ca II 8498/O I 8446 and Ca II 8498/Pa γ line ratios are close to or less than 1, and for the other group, they are larger than 5. For Gaia23bab, the Ca II 8498/O I 8446 line ratios are ~ 14.3 and ~ 12.4 , and the Ca II 8498/Pa γ line ratios are ~ 3.7 and ~ 4.5 for the LBT and the IRTF epochs, respectively. Therefore, they are mostly consistent with the second group mentioned by J. Kwan & W. Fischer (2011), and require H densities of $\sim 10^{12}$ cm^{-3} and temperatures $\lesssim 7500$ K. This higher density component compared to the results from the hydrogen lines may be related to the disk boundary layer, as Ca II line emission may also be related to that in addition to the accretion column (J. Kwan & W. Fischer 2011). In addition, the ratios of the Ca II triplet lines are close to 1 at both epochs, which implies that they are optically thick. According to the models of R. Azevedo et al. (2006), the 0.8542 μm line is the strongest, which is consistent with the observations for Gaia23bab.

4. Discussion

Here we compare the properties of Gaia23bab to those of other EXors and eruptive YSOs. The wavelengths of the Br γ and CO 2–0 lines are close enough that differences in veiling and extinction can be ignored. These diagnostics were previously used for other (eruptive) young stars (M. S. Connelley & T. P. Greene 2010; S. Park et al. 2021). In Figure 11, we compare the equivalent widths of the Br γ and CO 2–0 lines measured for Gaia23bab and other EXors. Another peculiar eruptive YSO, which represents an intermediate case between EXors and FUors, with an emission line spectrum (V899 Mon; S. Park et al. 2021) is also included, as well as the Class I type YSO IRAS 04239+2436 (T. P. Greene & C. J. Lada 1996). The general trend of increasing CO emission for increasing Br γ emission, which was already seen for other young stars (e.g., M. S. Connelley & T. P. Greene 2010), is also seen for the plotted EXors. Among the plotted examples, the equivalent widths of Gaia23bab are closest to those of IRAS 04239+2436

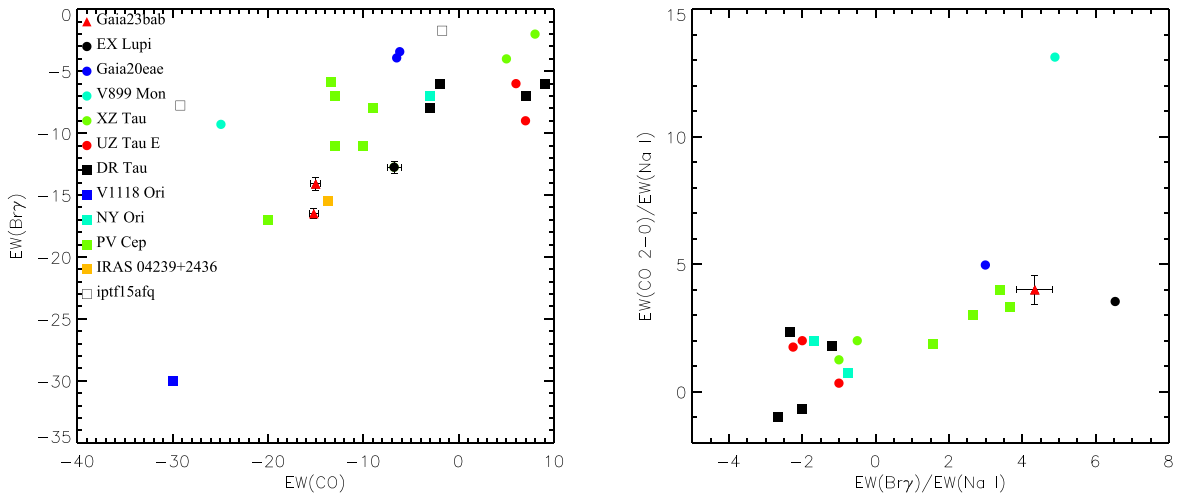


Figure 11. Comparison between the equivalent widths of the $\text{Br}\gamma$ line and the CO 2-0 line for EXOrs and other eruptive YSOs with an emission line spectrum. References: EX Lupi (Á. Kóspál et al. 2011), Gaia20eae (F. Cruz-Sáenz de Miera et al. 2022), V899 Mon (S. Park et al. 2021), XZ Tau, UZ Tau E, DR Tau, V1118 Ori, NY Ori, PV Cep (D. Lorenzetti et al. 2009), and IRAS 04239+2436 (T. P. Greene & C. J. Lada 1996).

(T. P. Greene & C. J. Lada 1996) and to PV Cep at some of the observed epochs (D. Lorenzetti et al. 2009).

Another key diagnostic of EXOrs is the Na I feature at $2.206 \mu\text{m}$. Given that it is close to the $\text{Br}\gamma$ and CO 2-0 lines, their flux ratios can be directly compared as they are not affected by extinction effects. The first ionization potential of sodium is low (5.1 eV); therefore, it can be present near low-mass late-type stars, such as CTTS and EXOrs, and in regions that are shielded from ionizing photons around earlier-type stars, such as in disks. As hydrogen is neutral in the Na^+ region, a low value of the $\text{Br}\gamma/\text{Na I}$ ratio suggests low ionization and the presence of higher density regions. In the right panel of Figure 11, we plot the CO 2-0/Na I ratio versus the $\text{Br}\gamma/\text{Na I}$ ratio for the same sample as used to compare the $\text{Br}\gamma$ and CO 2-0 equivalent widths. The CO 2-0/Na I is in the range between 2 and 5 for most EXOrs, including Gaia23bab. Most $\text{Br}\gamma/\text{Na I}$ ratios are also low, which was interpreted by D. Lorenzetti et al. (2009) as being because the role of the circumstellar disk dominates. Gaia23bab shows one of the highest CO 2-0/Na I as well as $\text{Br}\gamma/\text{Na I}$ ratios among the plotted sample. It is interesting to note that V899 Mon, a peculiar eruptive YSO with an emission line spectrum, has a CO 2-0/Na I ratio well above the range where most EXOrs are. In the case of the Class I type YSO IRAS 04239+2436, both the CO 2-0/Na I and the $\text{Br}\gamma/\text{Na I}$ ratios are outside of the range that most EXOrs in the figure represent.

In addition to its spectral features and accretion rate, the recurrence of the outbursts also points to an EXOr origin. In addition to the two well-defined outbursts seen in the light curves in Figure 1, another earlier outburst was identified in Pan-STARRS data between 2012 April and 2014 June (T. Giannini et al. 2024). As mentioned in Section 3.1 and in T. Giannini et al. (2024), the two outbursts seen in the Gaia light curve have a similar amplitude and color variation. A direct comparison of these two outbursts with the earlier one seen in the Pan-STARRS data is not possible due to the low number of data points, which do not allow for precisely deriving the amplitude and timescale of that earlier outburst. However, based on the parameters given in Table 1 of T. Giannini et al. (2024), this earlier outburst might also be comparable to the two outbursts seen in the Gaia light curve.

These two outbursts have different durations: comparing the FWHM values fitted to the light curves in Section 3.1, the 2023 brightening was a factor of 1.5–2 longer than the one in 2017.

According to the recent definition of accretion-related events by W. J. Fischer et al. (2023), the accretion events with an amplitude of 1–2.5 mag are referred to as bursts, while the accretion events with an amplitude above 2.5 mag are called outbursts. According to this definition, the brightening events of Gaia23bab are closer to bursts, as their amplitudes are only above 2.5 in ZTF bands (see Section 3.1 and T. Giannini et al. 2024). F. Cruz-Sáenz de Miera et al. (2023) present in their Figure 1 the long-term light curve of EX Lupi, the prototype of EXOrs. During the ~ 130 yr covered by the light curve, only three outbursts (according to the W. J. Fischer et al. 2023 definition) are seen, however, there are many—at least 19—bursts with similar amplitudes to those produced by Gaia23bab in 2017 and 2023. Other EXOrs with long-term light curves include VY Tau, which had 14 outbursts between 1940 and 1970 (G. H. Herbig 1990), as well as V1118 Ori, which had at least five outbursts over 30 yr (T. Giannini et al. 2020). In order to better constrain the timescales, amplitude, and recurrence timescales of EXOr (out)bursts, their long-term monitoring with ongoing and future surveys such as ZTF and the Legacy Survey of Space and Time is important.

5. Summary

We analyzed the physical properties of an EXOr, Gaia23bab, which was recently discovered based on Gaia Photometric Science Alerts. We studied its 2023 outburst using NIR spectra collected at three different epochs during the outburst. We also measured NIR and optical photometry during the outburst, and collected archival photometry, which included an earlier (2017) outburst of the target. Our main results can be summarized as follows:

ATLAS o and c data reveal a similar color evolution of the source during both the 2017 and the 2023 outbursts, which may partly be related to changes in circumstellar extinction.

The spectra obtained at the three epochs during the 2023 outburst all show typical EXOr signatures, with some apparent changes between the epochs, such as the nondetection of the

CO bandhead and the only tentative detection of the Na I doublet lines at the epoch during the fading of the source.

At two different epochs during the outburst, we found the accretion rate to be consistent with $\sim 2 \times 10^{-7} M_{\odot} \text{ yr}^{-1}$. A similar value was found by T. Giannini et al. (2024) for a third epoch during the outburst, suggesting that the accretion rate did not change significantly during the outburst.

A comparison of the fluxes of the Brackett series to predictions of Case B theory resulted in a best-fit temperature of 5000 K and a best-fit electron density was 10^9 cm^{-3} at the NOT and LBT epochs, and temperatures of 7500 and 10,000 K, and an electron density of 10^{10} cm^{-3} at the IRTF epoch. These values are consistent with earlier works on EXors and other types of eruptive YSOs.

In comparison to the predictions of the J. Kwan & W. Fischer (2011) model, the observed Balmer decrement is consistent with temperatures of 5000–12,500 K and a hydrogen density of 10^8 cm^{-3} . At the LBT and IRTF epochs, the fluxes of the Paschen series are closest to a model with n_{H} of 10^{11} cm^{-3} and are consistent with temperatures of 10,000–12,500 K.

The Ca II 8498/O I 8446 as well as the Ca II 8498/Pa γ line ratios are likely to trace a component with H densities of $\sim 10^{12} \text{ cm}^{-3}$ and temperatures $\lesssim 7500$ K, which may be related to the disk boundary layer.

Gaia23bab shows physical properties of a prototypical EXor, not only based on its accretion rate, but also based on the excitation conditions traced by its hydrogen lines. Monitoring its future outbursts will provide more information on how the physical conditions in a classical EXor change between outbursts.

Acknowledgments

We acknowledge the Hungarian National Research, Development and Innovation Office grant OTKA FK 146023. We acknowledge support from the ESA PRODEX contract No. 4000132054. G.M. and Z.N. were supported by the János Bolyai Research Scholarship of the Hungarian Academy of Sciences.

G.M. is funded by the European Union’s Horizon 2020 research and innovation program under grant agreement No. 101004141.

This work was also supported by the NKFIH NKKP grant ADVANCED 149943 and the NKFIH excellence grant TKP2021-NKTA-64. Project No. 149943 has been implemented with the support provided by the Ministry of Culture and Innovation of Hungary from the National Research, Development and Innovation Fund, financed under the NKKP ADVANCED funding scheme.

Based on observations made with the Nordic Optical Telescope, owned in collaboration by the University of Turku and Aarhus University, and operated jointly by Aarhus University, the University of Turku and the University of Oslo, representing Denmark, Finland, and Norway, the University of Iceland and Stockholm University at the Observatorio del Roque de los Muchachos, La Palma, Spain, of the Instituto de Astrofísica de Canarias.

This work was supported by the OPTICON-RadioNet Pilot (ORP) of the European Union’s Horizon 2020 research and innovation program under grant agreement No. 101004719.

This work has made use of data from the ATLAS project. The ATLAS project is primarily funded to search for near-

Earth asteroids through NASA grants NN12AR55G, 80NSSC18K0284, and 80NSSC18K1575; byproducts of the NEO search include images and catalogs from the survey area. This work was partially funded by Kepler/K2 grant J1944/80NSSC19K0112 and HST GO-15889, and STFC grants ST/T000198/1 and ST/S006109/1. The ATLAS science products have been made possible through the contributions of the University of Hawaii Institute for Astronomy, the Queen’s University Belfast, the Space Telescope Science Institute, the South African Astronomical Observatory, and the Millennium Institute of Astrophysics (MAS), Chile.

We acknowledge ESA Gaia, DPAC, and the Photometric Science Alerts Team.²⁰

BHTOM.space has been based on the open-source TOM Toolkit by LCO and has been developed with funding from the European Union’s Horizon 2020 and Horizon Europe research and innovation programmes under grant agreements No. 101004719 (OPTICON-RadioNet Pilot, ORP) and No. 101131928 (ACME).

The operation of the RC80 telescope was supported by the project GINOP 2.3.2-15-2016-00033 of the Hungarian Government, funded by the European Union.

This paper uses observations made at the Mount Suhora Astronomical Observatory, Poland.

This research was supported by the “SeismoLab” KKP-137523 élvonal grant of the Hungarian Research, Development and Innovation Office (NKFIH).

Z.B. was supported by the ÚNKP 22-2 New National Excellence Program of the Ministry for Culture and Innovation from the source of the National Research, Development and Innovation Fund.

B.S. and L.K. acknowledge the support of the Hungarian National Research, Development and Innovation Office grants KKP-143986 (élvonal). L.K. acknowledges the support of the Hungarian National Research, Development and Innovation Office grant OTKA PD-134784.

N.O.S. thanks the financial support provided by the undergraduate research assistant program of Konkoly Observatory.

Z.M.S. acknowledges funding from a St. Leonards scholarship from the University of St. Andrews. Z.M.S. is a member of the International Max Planck Research School (IMPRS) for Astronomy and Astrophysics at the Universities of Bonn and Cologne.

F.C.S.M. received financial support from the European Research Council (ERC) under the European Union’s Horizon 2020 research and innovation program (ERC Starting Grant “Chemtrip,” grant agreement No. 949278).

E.F. has been partially supported by project AYA2018-RTI-096188-B-I00 from the Spanish Agencia Estatal de Investigación and by grant agreement 101004719 of the EU project ORP.

Facilities: NOT, LBT, IRTF.

Appendix A Photometry

In Tables 3, 4, and 5 we present the photometry obtained with the Piszkestető RC80 and the Mount Suhora 60 cm telescopes.

²⁰ <https://gsaweb.ast.cam.ac.uk/alerts>

Table 3
RC80 Photometry of Gaia23bab

JD	<i>V</i>	<i>r</i>	<i>i</i>	JD	<i>V</i>	<i>r</i>	<i>i</i>
2460013.63	17.98 ± 0.15	17.15 ± 0.05	15.84 ± 0.03	2460194.37	19.56 ± 0.21	18.71 ± 0.07	17.15 ± 0.03
2460020.61	17.88 ± 0.08	17.00 ± 0.03	15.75 ± 0.02	2460195.42	19.96 ± 0.35	18.59 ± 0.09	17.03 ± 0.05
2460021.61	17.98 ± 0.33	17.37 ± 0.10	16.07 ± 0.04	2460196.35	19.77 ± 0.21	18.70 ± 0.07	17.10 ± 0.03
2460022.62	18.25 ± 0.09	17.38 ± 0.04	16.04 ± 0.02	2460197.39	19.76 ± 0.31	18.73 ± 0.09	17.18 ± 0.05
2460025.62	18.20 ± 0.10	17.16 ± 0.03	15.81 ± 0.02	2460198.41	19.79 ± 0.30	18.77 ± 0.12	17.16 ± 0.04
2460026.58	17.79 ± 0.07	16.87 ± 0.02	15.58 ± 0.02	2460200.38	19.56 ± 0.23	18.85 ± 0.11	17.14 ± 0.04
2460027.59	18.25 ± 1.35	17.02 ± 0.22	15.64 ± 0.09	2460205.36	20.05 ± 0.84	18.99 ± 0.17	17.18 ± 0.05
2460029.58	18.32 ± 0.19	17.29 ± 0.05	16.01 ± 0.03	2460217.36	20.32 ± 1.20	18.88 ± 0.19	17.16 ± 0.06
2460031.60	18.30 ± 0.13	17.34 ± 0.05	15.99 ± 0.02	2460220.35	19.87 ± 0.45	18.72 ± 0.11	17.16 ± 0.04
2460032.61	18.21 ± 0.13	17.31 ± 0.04	15.96 ± 0.02	2460224.34	20.55 ± 0.61	19.34 ± 0.15	17.46 ± 0.05
2460045.54	18.09 ± 0.14	17.07 ± 0.06	15.78 ± 0.03	2460226.30	19.41 ± 0.45	18.80 ± 0.23	17.24 ± 0.06
2460047.52	17.54 ± 0.24	16.81 ± 0.06	15.55 ± 0.02	2460236.29	19.84 ± 1.29	19.32 ± 0.63	17.63 ± 0.17
2460054.53	17.82 ± 0.08	17.00 ± 0.03	15.67 ± 0.05	2460430.50	20.97 ± 0.45	20.08 ± 0.16	17.75 ± 0.04
2460055.53	17.83 ± 0.07	16.93 ± 0.03	15.65 ± 0.02	2460431.53	22.64 ± 1.95	21.39 ± 0.47	17.84 ± 0.05
2460058.52	18.06 ± 0.11	17.14 ± 0.03	15.83 ± 0.02	2460432.55	21.87 ± 1.06	19.93 ± 0.15	17.80 ± 0.09
2460060.49	18.76 ± 1.03	17.14 ± 0.12	15.83 ± 0.07	2460449.47	21.36 ± 0.85	22.16 ± 1.38	18.06 ± 0.07
2460062.52	17.85 ± 0.08	16.96 ± 0.03	15.70 ± 0.02	2460461.52	21.71 ± 0.78	21.82 ± 0.73	17.95 ± 0.09
2460064.56	18.13 ± 0.07	17.20 ± 0.04	15.88 ± 0.02	2460478.50	20.66 ± 0.79	20.01 ± 0.24	17.81 ± 0.05
2460065.50	18.06 ± 0.09	17.20 ± 0.03	15.85 ± 0.02	2460479.44	20.80 ± 0.38	20.21 ± 0.18	17.81 ± 0.04
2460069.50	18.19 ± 0.18	17.19 ± 0.07	15.92 ± 0.03	2460480.40	21.36 ± 0.84	22.31 ± 1.84	16.97 ± 1.28
2460097.53	18.03 ± 0.05	17.14 ± 0.03	15.80 ± 0.02	2460481.41	20.49 ± 0.46	20.13 ± 0.26	17.68 ± 0.05
2460098.50	18.00 ± 0.14	17.14 ± 0.05	15.78 ± 0.02	2460486.49	...	20.32 ± 0.26	17.82 ± 0.06
2460099.51	18.12 ± 0.11	17.32 ± 0.04	15.94 ± 0.02	2460497.49	21.28 ± 0.45	20.21 ± 0.15	17.86 ± 0.04
2460109.53	18.14 ± 0.05	17.26 ± 0.03	15.96 ± 0.02	2460498.40	21.26 ± 0.46	20.35 ± 0.16	17.82 ± 0.03
2460110.48	18.13 ± 0.05	17.25 ± 0.03	15.94 ± 0.02	2460500.46	20.46 ± 0.24	19.73 ± 0.11	17.73 ± 0.03
2460113.48	18.58 ± 0.08	17.70 ± 0.03	16.31 ± 0.02	2460501.42	21.22 ± 0.51	20.12 ± 0.15	17.87 ± 0.04
2460114.55	18.77 ± 0.12	17.68 ± 0.06	16.25 ± 0.03	2460502.44	...	20.17 ± 0.40	17.80 ± 0.09
2460115.47	18.42 ± 0.07	17.49 ± 0.03	16.12 ± 0.02	2460503.45	21.42 ± 1.69	...	17.72 ± 0.26
2460116.51	18.38 ± 0.06	17.45 ± 0.03	16.09 ± 0.02	2460505.44	20.30 ± 0.42	19.36 ± 0.24	17.69 ± 0.07
2460118.51	17.68 ± 0.05	16.82 ± 0.02	15.55 ± 0.01	2460506.47	20.13 ± 0.23	19.92 ± 0.15	17.67 ± 0.05
2460122.50	17.78 ± 0.04	16.89 ± 0.02	15.58 ± 0.01	2460507.53	19.40 ± 0.45	20.69 ± 0.62	17.74 ± 0.08
2460126.45	17.95 ± 0.10	17.04 ± 0.03	15.72 ± 0.03	2460510.46	20.05 ± 0.36	20.15 ± 0.36	17.75 ± 0.07
2460128.39	17.75 ± 0.09	16.88 ± 0.04	15.58 ± 0.02	2460511.49	20.34 ± 1.00	19.45 ± 0.28	17.75 ± 0.09
2460135.42	18.83 ± 0.10	17.90 ± 0.04	16.55 ± 0.02	2460513.47	18.98 ± 0.38	18.41 ± 0.26	17.37 ± 0.20
2460137.56	18.75 ± 0.23	17.67 ± 0.09	16.36 ± 0.09	2460514.53	...	19.58 ± 0.38	17.80 ± 0.11
2460141.40	19.16 ± 0.13	18.18 ± 0.05	16.70 ± 0.03	2460516.47	...	21.66 ± 1.27	17.93 ± 0.11
2460143.41	18.53 ± 0.09	17.63 ± 0.03	16.27 ± 0.02	2460518.49	20.73 ± 0.36	20.87 ± 0.32	18.03 ± 0.06
2460145.43	18.75 ± 0.10	17.80 ± 0.05	16.40 ± 0.02	2460519.48	21.66 ± 0.77	19.83 ± 0.13	17.94 ± 0.07
2460146.38	18.54 ± 0.10	17.75 ± 0.04	16.39 ± 0.02	2460520.49	...	20.37 ± 0.27	17.97 ± 0.07
2460171.42	18.74 ± 0.07	17.80 ± 0.03	16.45 ± 0.02	2460521.52	20.66 ± 0.43	20.19 ± 0.21	17.82 ± 0.04
2460177.38	18.92 ± 0.12	18.11 ± 0.04	16.68 ± 0.02	2460522.48	21.45 ± 0.66	20.08 ± 0.14	17.90 ± 0.05
2460178.38	19.10 ± 0.15	18.19 ± 0.06	16.70 ± 0.04	2460523.52	19.77 ± 0.57	19.80 ± 0.53	18.10 ± 0.21
2460179.46	19.53 ± 0.57	18.28 ± 0.15	16.75 ± 0.05	2460526.47	20.80 ± 0.71	19.92 ± 0.25	18.11 ± 0.08
2460180.39	18.90 ± 0.13	17.97 ± 0.05	16.60 ± 0.02	2460528.51	19.50 ± 0.16	20.02 ± 0.18	17.98 ± 0.06
2460181.40	19.14 ± 0.12	18.22 ± 0.06	16.80 ± 0.04	2460530.47	19.09 ± 1.72	18.97 ± 1.36	17.06 ± 0.58
2460182.37	19.06 ± 0.12	18.18 ± 0.05	16.76 ± 0.02	2460532.51	20.06 ± 0.23	20.82 ± 0.32	17.95 ± 0.07
2460184.39	19.06 ± 0.23	18.17 ± 0.12	16.81 ± 0.07	2460533.43	21.19 ± 0.44	20.06 ± 0.13	17.91 ± 0.04
2460193.37	19.99 ± 0.30	19.02 ± 0.10	17.27 ± 0.04	2460534.42	...	20.16 ± 0.29	17.93 ± 0.08

Table 4
RC80 Photometry of Gaia23bab

JD	<i>V</i>	<i>r</i>	<i>i</i>
2460536.47	22.11 ± 1.41	20.01 ± 0.18	17.88 ± 0.09
2460537.45	...	19.75 ± 0.31	17.73 ± 0.07
2460538.45	22.61 ± 2.07	20.17 ± 0.18	17.78 ± 0.11
2460539.46	...	20.02 ± 0.20	17.90 ± 0.07
2460545.42	21.35 ± 0.99	19.45 ± 0.16	17.71 ± 0.08
2460546.41	20.70 ± 0.43	19.83 ± 0.15	17.77 ± 0.04
2460547.45	20.26 ± 0.44	19.94 ± 0.30	17.89 ± 0.07
2460548.44	21.50 ± 1.26	21.86 ± 1.68	18.00 ± 0.08
2460551.44	20.40 ± 0.53	20.06 ± 0.27	18.98 ± 0.14
2460552.44	20.47 ± 0.31	20.01 ± 0.17	17.82 ± 0.04
2460553.45	21.73 ± 1.21	20.01 ± 0.18	18.04 ± 0.09
2460554.43	19.87 ± 0.69	20.25 ± 0.52	17.80 ± 0.09
2460558.42	21.50 ± 1.11	20.24 ± 0.27	17.88 ± 0.06

Table 5
Mt Suhora Photometry of Gaia23bab

MJD	<i>V</i>	<i>R</i>	<i>I</i>
60020.15	17.73 ± 0.03	16.41 ± 0.02	14.91 ± 0.02
60021.13	18.18 ± 0.06	16.97 ± 0.06	15.34 ± 0.05
60062.07	17.69 ± 0.04	16.52 ± 0.05	15.08 ± 0.04
60076.05	17.92 ± 0.04	16.67 ± 0.04	15.26 ± 0.03
60092.03	17.91 ± 0.05	16.50 ± 0.02	15.21 ± 0.04
60139.97	18.53 ± 0.13	17.32 ± 0.08	15.65 ± 0.05
60140.03	18.72 ± 0.09	17.49 ± 0.07	15.76 ± 0.05
60144.01	18.30 ± 0.06	16.98 ± 0.05	15.55 ± 0.05
60145.00	18.42 ± 0.06	17.12 ± 0.05	15.65 ± 0.05
60145.98	18.35 ± 0.05	17.08 ± 0.03	15.60 ± 0.03
60153.88	18.22 ± 0.08	16.79 ± 0.03	15.35 ± 0.03
60164.85	18.05 ± 0.04	16.58 ± 0.02	15.32 ± 0.04
60166.89	18.08 ± 0.03	16.81 ± 0.03	15.45 ± 0.04
60170.88	18.58 ± 0.07	17.38 ± 0.08	15.81 ± 0.06
60171.83	18.58 ± 0.07	17.18 ± 0.06	15.61 ± 0.03
60179.97	18.61 ± 0.11	17.26 ± 0.05	15.52 ± 0.04
60180.97	18.96 ± 0.08	17.44 ± 0.03	15.67 ± 0.03
60193.83	19.56 ± 0.09	18.00 ± 0.05	16.17 ± 0.05
60215.86	...	17.93 ± 0.10	15.98 ± 0.04
60216.78	...	18.02 ± 0.08	15.95 ± 0.04
60221.77	19.79 ± 0.27	18.02 ± 0.07	16.23 ± 0.04
60234.75	19.90 ± 0.15	18.32 ± 0.08	16.59 ± 0.07
60255.72	20.06 ± 0.19	18.23 ± 0.07	16.13 ± 0.06
60497.92	21.18 ± 0.29	19.07 ± 0.11	16.79 ± 0.10
60528.86	20.71 ± 0.15	19.25 ± 0.10	17.10 ± 0.12

Appendix B

Line Identification

In Figures 12 and 13 we show the NOT, LBT and IRTF spectra with the identified lines. In Figures 14 and 15 we show the profiles of the detected HI lines.

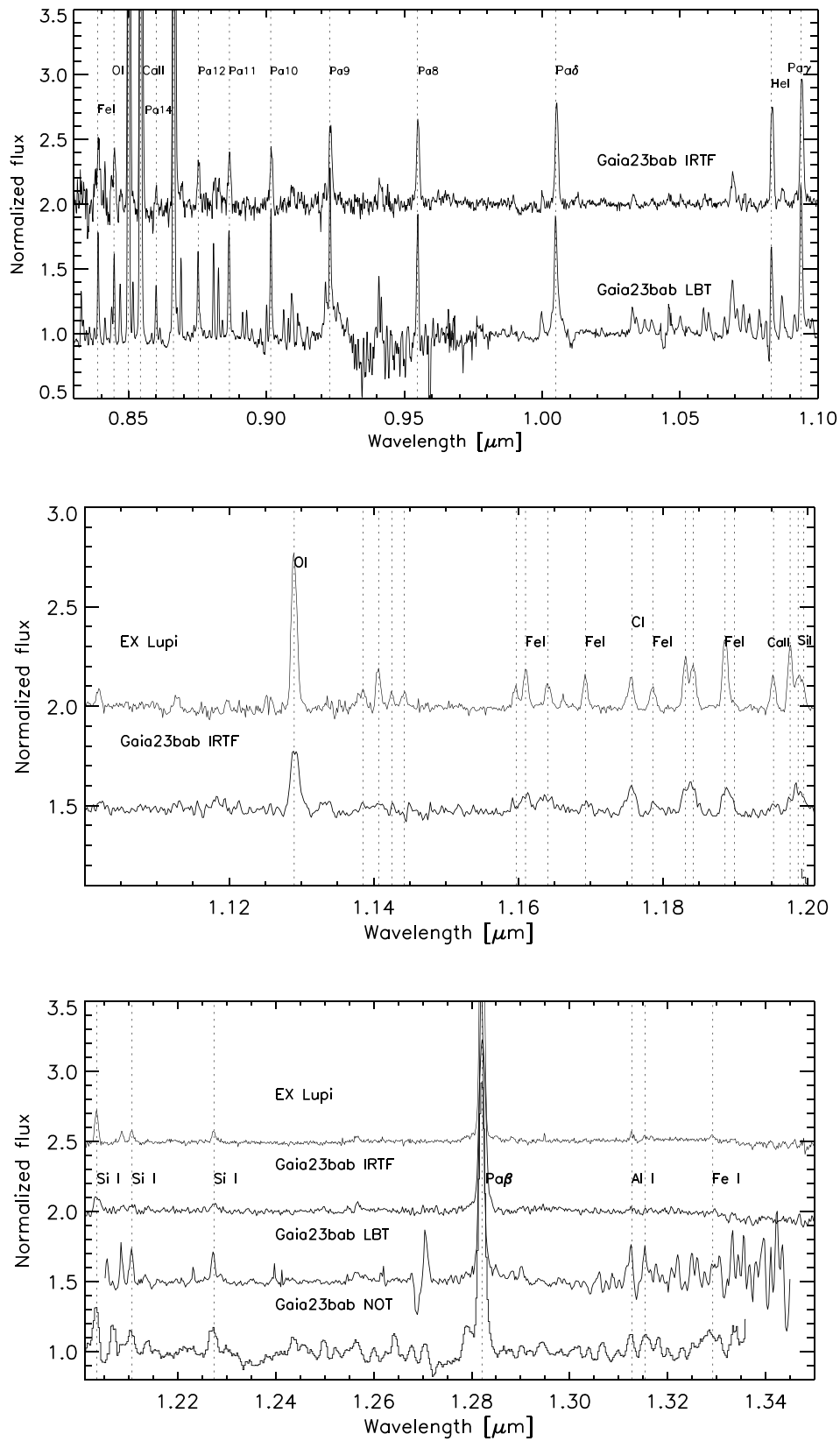


Figure 12. Comparison of the NOT and IRTF spectra to those of EX Lupi during its outburst (Á. Kóspál et al. 2011).

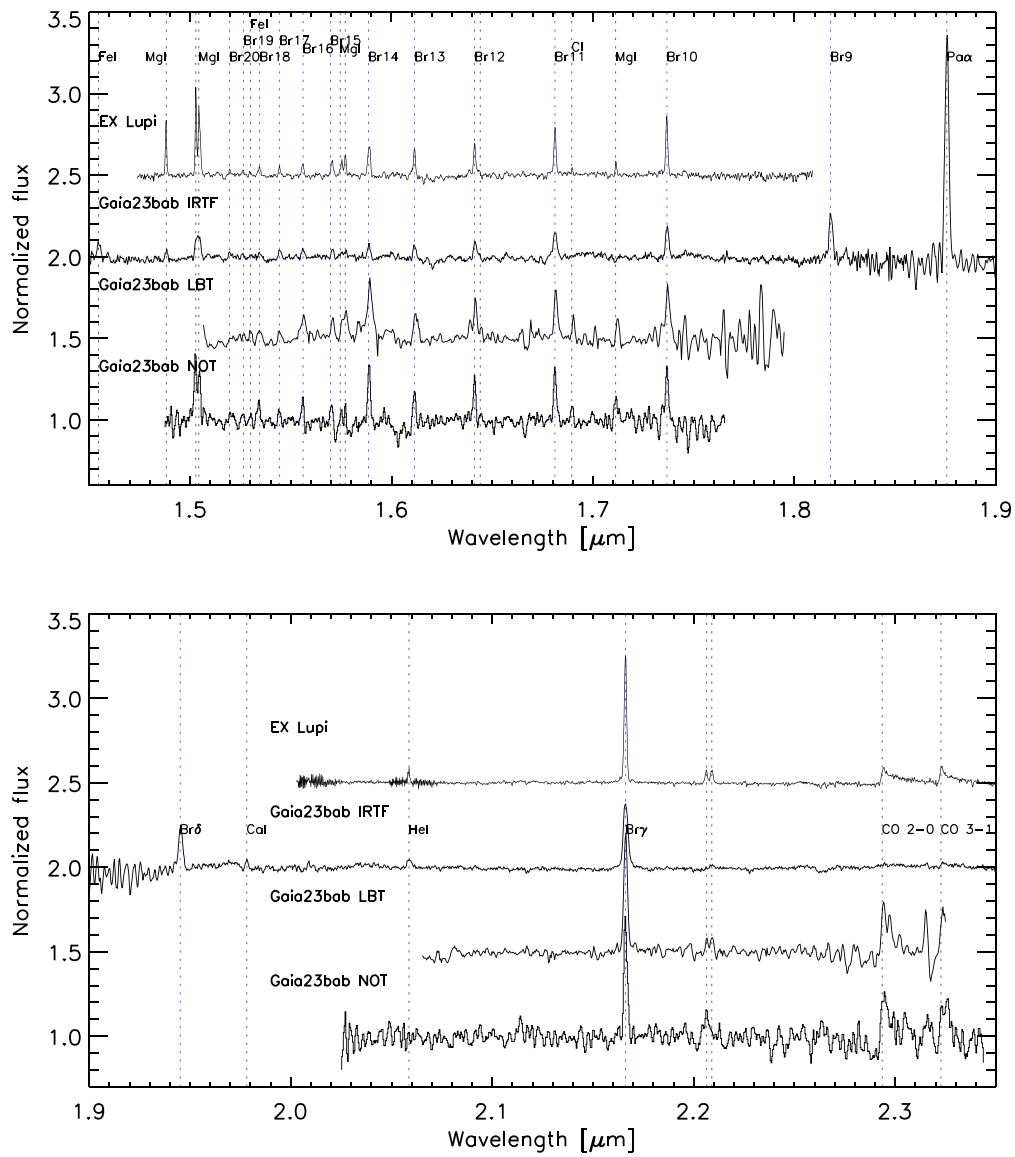


Figure 13. Comparison of the NOT and IRTF spectra to those of EX Lupi during its outburst (Á. Kóspál et al. 2011).

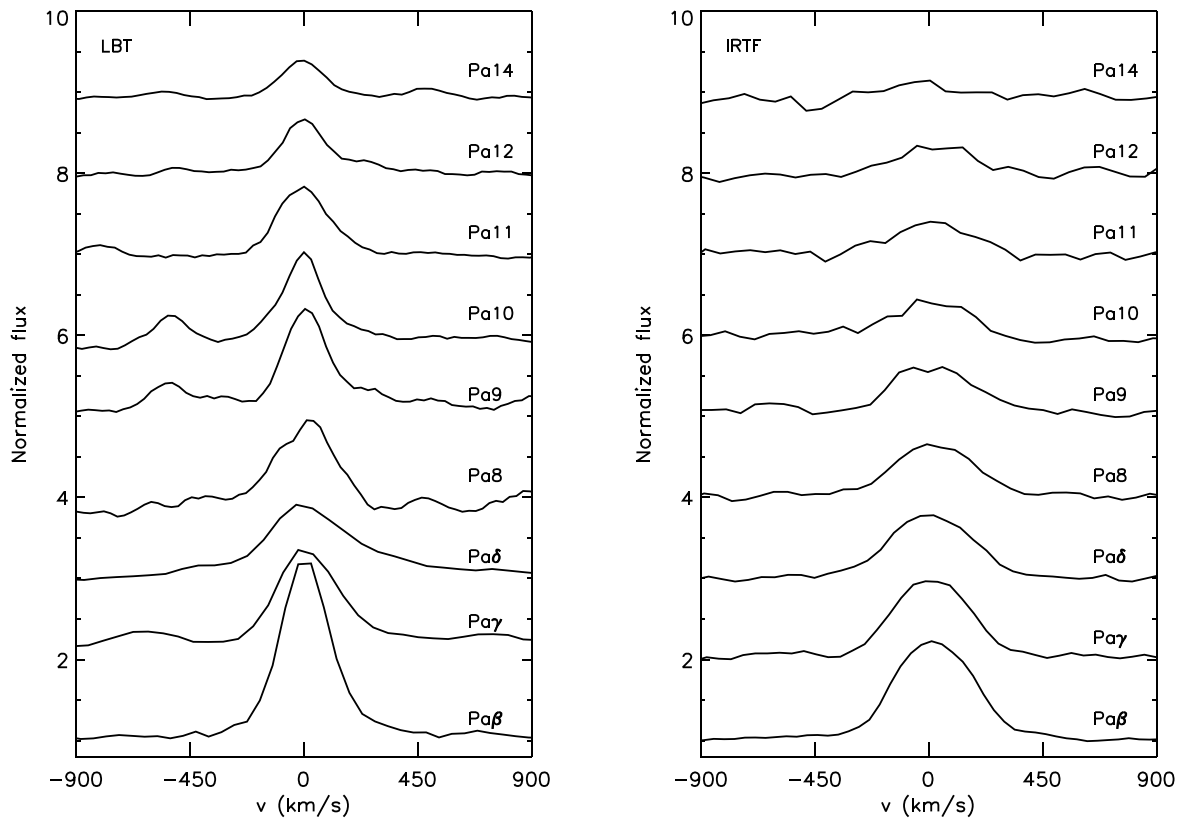


Figure 14. The H I Paschen lines detected in the spectra of Gaia23bab.

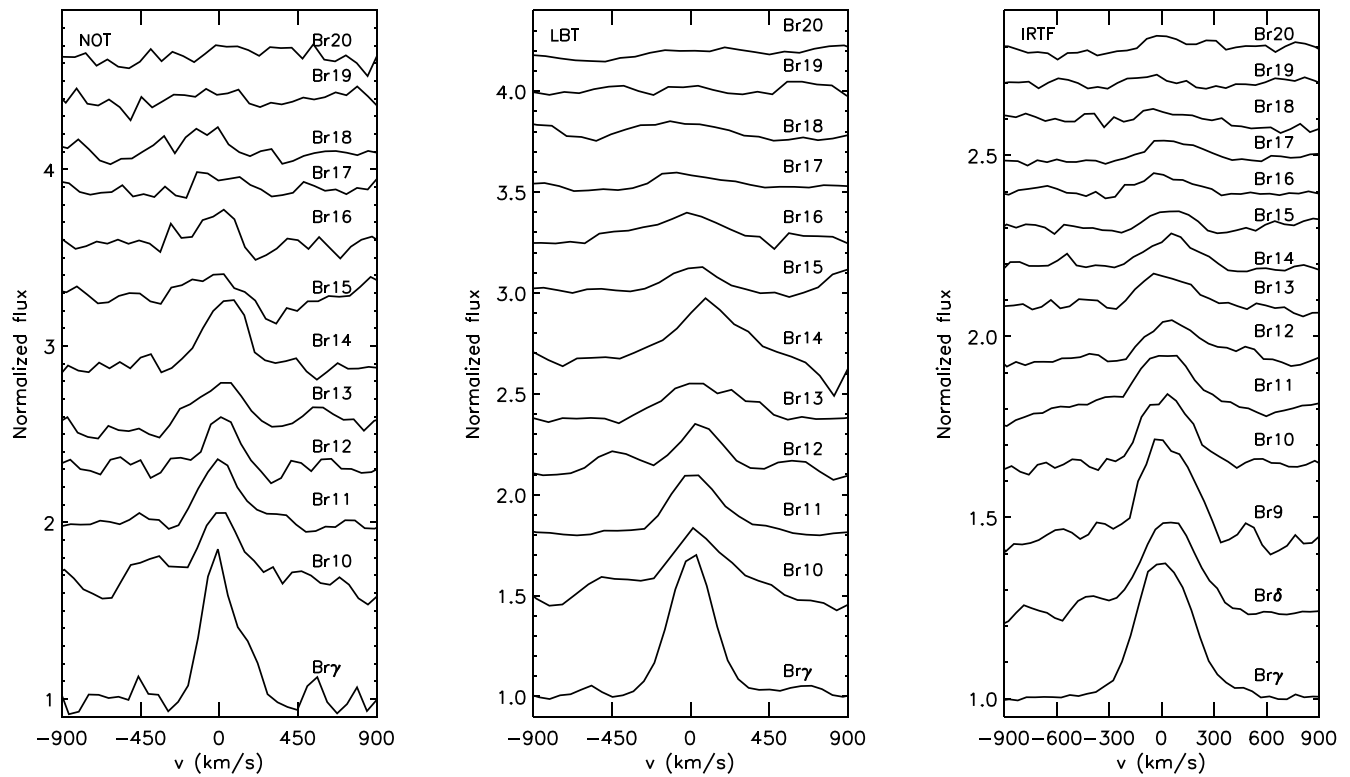


Figure 15. The H I Brackett lines detected in the spectra of Gaia23bab.

Appendix C Line Parameters

In Tables 6 and 7 we present the list of spectral features detected at each epoch, and their equivalent widths.

Table 6
Equivalent Widths of the Spectral Features Detected at the LBT and IRTF Epochs

Species	λ_{tab} (μm)	EW(LBT) (\AA)	EW(IRTF) (\AA)
Fe I	0.8388	-4.8 ± 0.2	-7.5 ± 0.5
O I	0.8446	-3.5 ± 0.1	-5.0 ± 0.5
Ca II	0.8498	-50.0 ± 1.0	-62.0 ± 2.0
Ca II	0.8542	-54.0 ± 1.0	-69.0 ± 1.0
Ca II	0.8662	-53.5 ± 2.0	-62.0 ± 2.0
H I (Pa14)	0.8601	-0.9 ± 0.3	-0.9 ± 0.1
H I (Pa13)*	0.8667	-1.9 ± 0.4	-2.0 ± 0.3
H I (Pa12)	0.8753	-4.2 ± 0.3	-4.1 ± 0.3
H I (Pa11)	0.8865	-6.1 ± 0.3	-4.7 ± 0.5
H I (Pa10)	0.9015	-6.2 ± 0.3	-4.9 ± 0.3
H I (Pa9)*	0.9232	-9.4 ± 0.5	-7.5 ± 0.1
H I (Pa8)	0.9546	-8.8 ± 0.2	-7.5 ± 0.3
H I (Pa δ)	1.0052	-12.5 ± 0.6	-11.3 ± 0.5
He I	1.0830	-7.0 ± 0.4	-10.0 ± 0.1
H I (Pa γ)	1.0941	-13.6 ± 0.5	-13.5 ± 0.3
O I	1.1290	...	-4.7 ± 0.3
Fe I	1.1610	...	-1.1 ± 0.1
Fe I	1.1641	...	-1.9 ± 0.1
Fe I	1.1693	...	-1.0 ± 0.2
C I	1.1757	...	-1.9 ± 0.1
Fe I	1.1786	...	-0.8 ± 0.2
Mg I	1.1831	...	-3.1 ± 0.1

Note. The lines marked with * are most likely blended at least at one of the epochs. Lines for which no equivalent widths are provided are either not covered by the data (...).

Table 7
Equivalent Widths of the Spectral Features Detected at the NOT, LBT, and IRTF Epochs

Species	λ_{tab} (μm)	EW(NOT) (\AA)	EW(LBT) (\AA)	EW(IRTF) (\AA)
Si I	1.2035	-4.4 ± 0.1	-2.2 ± 0.1	-1.8 ± 0.2
Si I	1.2274	-3.0 ± 0.2	-1.9 ± 0.2	-0.9 ± 0.1
H I (Pa β)	1.2821	-31.0 ± 2.0	-25.0 ± 0.6	-21.5 ± 0.2
Al I	1.3127	-2.9 ± 0.2	-2.5 ± 0.2	...
Al I	1.3154	-3.1 ± 0.2	-2.4 ± 0.2	...
Fe I	1.4547	-1.9 ± 0.2
Mg I	1.4882	-0.9 ± 0.1
Mg I	1.5029	-5.4 ± 0.3
Mg I	1.5044	-5.6 ± 0.3
H I (Br20)	1.5195	-1.2 ± 0.2	-0.8 ± 0.2	-0.4 ± 0.1
H I (Br19)	1.5265	-1.3 ± 0.2	-1.3 ± 0.2	-0.5 ± 0.1
Fe I	1.5299	-1.6 ± 0.1	-0.6 ± 0.2	-0.5 ± 0.1
H I (Br18)	1.5346	-1.7 ± 0.2	-1.8 ± 0.2	-0.6 ± 0.1
H I (Br17)	1.5443	-1.8 ± 0.2	-1.9 ± 0.2	-0.9 ± 0.1
H I (Br16)	1.5561	-2.3 ± 0.2	-2.8 ± 0.2	-1.0 ± 0.1
H I (Br15)	1.5705	-2.6 ± 0.2	-2.8 ± 0.3	-1.1 ± 0.1
Mg I*	1.5745	-2.1 ± 0.2
Mg I*	1.5770	-1.8 ± 0.2
H I (Br14)*	1.5885	-6.3 ± 0.2	-10.3 ± 0.3	-1.8 ± 0.1
H I (Br13)	1.6114	-4.0 ± 0.2	-5.1 ± 0.2	-1.8 ± 0.1
H I (Br12)*	1.6412	-4.6 ± 0.1	-5.5 ± 0.3	-2.4 ± 0.2
H I (Br11)	1.6811	-5.2 ± 0.2	-6.3 ± 0.2	-3.2 ± 0.2
H I (Br10)	1.7367	-6.4 ± 0.2	-7.6 ± 0.3	-4.3 ± 0.2
H I (Br9)	1.8179	-6.7 ± 0.2
H I (Pa α)	1.8756	-34.0 ± 1.0
H I (Br δ)	1.9451	-6.8 ± 0.2
Ca I	1.9782	-0.9 ± 0.1
He I	2.0587	-1.2 ± 0.1
Na I	2.2062	...	-1.6 ± 0.2	...
Na I	2.2090	...	-2.2 ± 0.2	...
H I (Br γ)	2.1661	-14.1 ± 0.5	-16.5 ± 0.4	-11.0 ± 1.0
CO 2-0	2.2992	-15.0 ± 0.5	-15.2 ± 0.5	...

Note. The lines marked with * are most likely blended at least at one of the epochs. Lines for which no equivalent widths are provided are either not covered by the data (...) or cannot be derived as it is either not detected or is blended (...).

ORCID iDs

Zsófia Nagy  <https://orcid.org/0000-0002-3632-1194>
 Ágnes Kóspál  <https://orcid.org/0000-0001-7157-6275>
 Péter Ábrahám  <https://orcid.org/0000-0001-6015-646X>
 Teresa Giannini  <https://orcid.org/0000-0002-7035-8513>
 Mária Kun  <https://orcid.org/0000-0002-7538-5166>
 Manuele Gangi  <https://orcid.org/0000-0002-8364-7795>
 Fernando Cruz-Sáenz de Miera  <https://orcid.org/0000-0002-4283-2185>
 Michael Kuhn  <https://orcid.org/0000-0002-0631-7514>
 Michał Siwak  <https://orcid.org/0000-0001-5018-3560>
 Máté Szilágyi  <https://orcid.org/0000-0002-3648-433X>
 Eleonora Fiorellino  <https://orcid.org/0000-0002-5261-6216>
 Simone Antonucci  <https://orcid.org/0000-0002-0666-3847>
 Katia Biazzo  <https://orcid.org/0000-0002-1892-2180>
 Attila Bódi  <https://orcid.org/0000-0002-8585-4544>
 Zsófia Bora  <https://orcid.org/0000-0001-6232-9352>
 Borbála Cseh  <https://orcid.org/0000-0002-6497-8863>
 Marek Drózdź  <https://orcid.org/0000-0001-9587-1615>
 András Péter Joó  <https://orcid.org/0000-0001-5203-434X>
 Csilla Kalup  <https://orcid.org/0000-0002-1663-0707>
 Gábor Marton  <https://orcid.org/0000-0002-1326-1686>
 Przemysław J. Mikołajczyk  <https://orcid.org/0000-0001-8916-8050>
 Brunella Nisini  <https://orcid.org/0000-0002-9190-0113>
 András Pál  <https://orcid.org/0000-0001-5449-2467>
 Bálint Seli  <https://orcid.org/0000-0002-3658-2175>
 Ádám Sódor  <https://orcid.org/0000-0001-7806-2883>
 László Szabados  <https://orcid.org/0000-0002-2046-4131>
 Zsófia Marianna Szabó  <https://orcid.org/0000-0001-9830-3509>
 Róbert Szakáts  <https://orcid.org/0000-0002-1698-605X>
 József Vinkó  <https://orcid.org/0000-0001-8764-7832>
 Łukasz Wyrzykowski  <https://orcid.org/0000-0002-9658-6151>
 Paweł Zieliński  <https://orcid.org/0000-0001-6434-9429>

References

Alcalá, J. M., Manara, C. F., Natta, A., et al. 2017, *A&A*, 600, A20
 Audard, M., Ábrahám, P., Dunham, M. M., et al. 2014, in *Protostars and Planets VI*, ed. H. Beuther et al. (Tucson, AZ: Univ. Arizona Press), 387
 Azevedo, R., Calvet, N., Hartmann, L., et al. 2006, *A&A*, 456, 225
 Bary, J. S., Matt, S. P., Skrutskie, M. F., et al. 2008, *ApJ*, 687, 376
 Bessell, M. S., & Brett, J. M. 1988, *PASP*, 100, 1134
 Cardelli, J. A., Clayton, G. C., & Mathis, J. S. 1989, *ApJ*, 345, 245
 Connelley, M. S., & Greene, T. P. 2010, *AJ*, 140, 1214
 Cruz-Sáenz de Miera, F., Kóspál, Á., Ábrahám, P., et al. 2022, *ApJ*, 927, 125
 Cruz-Sáenz de Miera, F., Kóspál, Á., Ábrahám, P., et al. 2023, *A&A*, 678, A88
 Cushing, M. C., Vacca, W. D., & Rayner, J. T. 2004, *PASP*, 116, 362
 Cutri, R. M., Skrutskie, M. F., van Dyk, S., et al. 2003, *The IRSA 2MASS All-Sky Point Source Catalog*, NASA/IPAC Infrared Science Archive (Washington, DC: NASA)
 Edwards, S., Kwan, J., Fischer, W., et al. 2013, *ApJ*, 778, 148

Fiorellino, E., Ábrahám, P., Kóspál, Á., et al. 2024, *A&A*, 686, A160
 Fischer, W. J., Hillenbrand, L. A., Herczeg, G. J., et al. 2023, in *ASP Conf. Ser. 534, Protostars and Planets VII*, ed. S. Inutsuka et al. (San Francisco, CA: ASP), 355
 Gaia Collaboration, Vallenari, A., Brown, A. G. A., et al. 2023, *A&A*, 674, A1
 Ghosh, A., Sharma, S., Ninan, J. P., et al. 2022, *ApJ*, 926, 68
 Giannini, T., Giunta, A., Gangi, M., et al. 2022, *ApJ*, 929, 129
 Giannini, T., Giunta, A., Lorenzetti, D., et al. 2020, *A&A*, 637, A83
 Giannini, T., Schisano, E., Nisini, B., et al. 2024, *ApJ*, 967, 41
 Greene, T. P., & Lada, C. J. 1996, *ApJ*, 461, 345
 Hartmann, L., Calvet, N., Gullbring, E., & D'Alessio, P. 1998, *ApJ*, 495, 385
 Hartmann, L., & Kenyon, S. J. 1996, *ARA&A*, 34, 207
 Heinze, A. N., Tonry, J. L., Denneau, L., et al. 2018, *AJ*, 156, 241
 Henden, A. A., Levine, S., Terrell, D., & Welch, D. L. 2015, *AAS Meeting*, 225, 336.16
 Herbig, G. H. 1977, *ApJ*, 217, 693
 Herbig, G. H. 1990, *ApJ*, 360, 639
 Herbig, G. H. 2008, *AJ*, 135, 637
 Hillenbrand, L. A., Contreras Peña, C., Morrell, S., et al. 2018, *ApJ*, 869, 146
 Hillenbrand, L. A., Reipurth, B., Connelley, M., Cutri, R. M., & Isaacson, H. 2019, *AJ*, 158, 240
 Hodapp, K. W., Denneau, L., Tucker, M., et al. 2020, *AJ*, 160, 164
 Hodapp, K. W., Reipurth, B., Petersson, B., et al. 2019, *AJ*, 158, 241
 Hodgkin, S. T., Harrison, D. L., Breedt, E., et al. 2021, *A&A*, 652, A76
 Hummer, D. G., & Storey, P. J. 1987, *MNRAS*, 224, 801
 Jayasinghe, T., Stanek, K. Z., Kochanek, C. S., et al. 2019, *MNRAS*, 485, 961
 Kóspál, Á., Ábrahám, P., Goto, M., et al. 2011, *ApJ*, 736, 72
 Kraus, S., Monnier, J. D., Che, X., et al. 2012, *ApJ*, 744, 19
 Kuhn, M. A., Benjamin, R. A., Ishida, E. E. O., et al. 2023, *RNAAS*, 7, 57
 Kuhn, M. A., de Souza, R. S., Krone-Martins, A., et al. 2021, *ApJS*, 254, 33
 Kuhn, M. A., Hillenbrand, L. A., Connelley, M. S., et al. 2024, *MNRAS*, 529, 2630
 Kwan, J., & Fischer, W. 2011, *MNRAS*, 411, 2383
 Lorenzetti, D., Larionov, V. M., Giannini, T., et al. 2009, *ApJ*, 693, 1056
 Mainzer, A., Bauer, J., Grav, T., et al. 2011, *ApJ*, 731, 53
 Mamajek, E. E., Torres, G., Prsa, A., et al. 2015, arXiv:1510.06262
 Martin, S. C. 1996, *ApJ*, 470, 537
 Marton, G., Tóth, L. V., Paladini, R., et al. 2016, *MNRAS*, 458, 3479
 Masci, F. J., Laher, R. R., Rusholme, B., et al. 2019, *PASP*, 131, 018003
 Megeath, S. T., Gutermuth, R., Muzerolle, J., et al. 2012, *AJ*, 144, 192
 Meyer, M. R., Calvet, N., & Hillenbrand, L. A. 1997, *AJ*, 114, 288
 Muzerolle, J., Calvet, N., & Hartmann, L. 2001, *ApJ*, 550, 944
 Nagy, Z., Ábrahám, P., Kóspál, Á., et al. 2022, *MNRAS*, 515, 1774
 Nagy, Z., Park, S., Ábrahám, P., et al. 2023, *MNRAS*, 524, 3344
 Nisini, B., Antonucci, S., & Giannini, T. 2004, *A&A*, 421, 187
 Park, S., Kóspál, Á., Ábrahám, P., et al. 2022, *ApJ*, 941, 165
 Park, S., Kóspál, Á., Cruz-Sáenz de Miera, F., et al. 2021, *ApJ*, 923, 171
 Pecaut, M. J., & Mamajek, E. E. 2013, *ApJS*, 208, 9
 Podio, L., Garcia, P. J. V., Bacciotti, F., et al. 2008, *A&A*, 480, 421
 Rayner, J. T., Toomey, D. W., Onaka, P. M., et al. 2003, *PASP*, 115, 362
 Shappee, B. J., Prieto, J. L., Grupe, D., et al. 2014, *ApJ*, 788, 48
 Shingles, L., Smith, K. W., Young, D. R., et al. 2021, *TNSAN*, 7, 1
 Siess, L., Dufour, E., & Forestini, M. 2000, *A&A*, 358, 593
 Siwak, M., Hillenbrand, L. A., Kóspál, Á., et al. 2023, *MNRAS*, 524, 5548
 Smith, K. W., Smartt, S. J., Young, D. R., et al. 2020, *PASP*, 132, 085002
 Szegedi-Elek, E., Ábrahám, P., Wyrzykowski, Ł., et al. 2020, *ApJ*, 899, 130
 Szilágyi, M., Kun, M., & Ábrahám, P. 2021, *MNRAS*, 505, 5164
 Tody, D. 1986, *Proc. SPIE*, 627, 733
 Tonry, J. L., Denneau, L., Heinze, A. N., et al. 2018, *PASP*, 130, 064505
 Vacca, W. D., Cushing, M. C., & Rayner, J. T. 2003, *PASP*, 115, 389
 Vacca, W. D., & Sandell, G. 2011, *ApJ*, 732, 8
 Whelan, E. T., Bonito, R., Antonucci, S., et al. 2014, *A&A*, 565, A80
 Wright, E. L., Eisenhardt, P. R. M., Mainzer, A. K., et al. 2010, *AJ*, 140, 1868